

**How well do multi-satellite products capture the space-time dynamics of precipitation?**

**Part I: five products assessed via a wavenumber-frequency decomposition**

Clement Guilloteau<sup>1,\*</sup>, Efi Foufoula-Georgiou<sup>1,2</sup>, Pierre Kirstetter<sup>3,4</sup>, Jackson Tan<sup>5,6</sup>, and George  
J. Huffman<sup>5</sup>

<sup>1</sup>Department of Civil and Environmental Engineering, University of California, Irvine

<sup>2</sup>Department of Earth System Science, University of California, Irvine

<sup>3</sup>Hydrometeorology and Remote Sensing Laboratory, University of Oklahoma, Norman

<sup>4</sup>NOAA Severe Storms Laboratory, Norman, Oklahoma

<sup>5</sup>NASA Goddard Space Flight Center, Greenbelt, Maryland

<sup>6</sup>Universities Space Research Association, Columbia, Maryland

\*cguillot@uci.edu

**Abstract**

As more global satellite-derived precipitation products become available, it is imperative to evaluate them more carefully for providing guidance as to how well precipitation space-time features are captured for use in hydrologic modeling, climate studies and other applications. Here

we propose a space-time Fourier spectral analysis and define a suite of metrics which evaluate the spatial organization of storm systems, the propagation speed and direction of precipitation features, and the space-time scales at which a satellite product reproduces the variability of a reference “ground-truth” product (“effective resolution”). We demonstrate how the methodology relates to our physical intuition using the case study of a storm system with rich space-time structure. We then evaluate five high-resolution multi-satellite products (CMORPH, GSMaP, IMERG-early, IMERG-final and PERSIANN-CCS) over a period of two years over the southeastern US. All five satellite products show generally consistent space-time power spectral density when compared to a reference ground gauge-radar dataset (GV-MRMS), revealing agreement in terms of average morphology and dynamics of precipitation systems. However, a deficit of spectral power at wavelengths shorter than 200 km and periods shorter than 4 h reveals that all satellite products are excessively “smooth”. The products also show low levels of spectral coherence with the gauge-radar reference at these fine scales, revealing discrepancies in capturing the location and timing of precipitation features. From the space-time spectral coherence, the IMERG-final product shows superior ability in resolving the space-time dynamics of precipitation down to 200 km and 4 h scales compared to the other products.

### **Significance statement**

Precipitation estimation products are essential for understanding water cycle dynamics and climate change, and for decision support in regions lacking ground observations. Several global products exist from multiple satellites orbiting the earth, but the challenge remains that of evaluating these products for accuracy and for improving the retrieval algorithms. Here we posit that the classical “pixel-to-pixel” comparison is not adequate and propose an approach that focuses

on comparing space-time dynamics through a Fourier spectral analysis, which provides information about the size, shape and orientation of precipitation systems as well as their motion speed and direction. We evaluate five state-of-the-art multi-satellite products and identify shortcomings, in particular in their ability to capture the sub-mesoscale variability of precipitation.

## **1. Introduction**

Satellite-derived Quantitative Precipitation Estimation (QPE) products have been around for several decades and are now commonly used in climate studies (Mehta and Yang 2008, Roca et al. 2014, Kerns and Chen 2020), hydrologic modeling and prediction (Casse and Gosset 2015) and various other applications (Kirschbaum et al. 2017) including vegetation monitoring (Hilker et al. 2014, Suepa et al. 2016), landslide risk management (Kirschbaum and Stanley 2018), health risk management (Guilloteau et al. 2014), etc. Extensive literature exists on evaluating and validating satellite products (e.g., Sapiano and Arkin 2009, Derin et al. 2016, Beck et al. 2019). In all of these evaluation or validation efforts, the satellite products must be compared with a “truth”, typically, a ground reference measurement, such as from raingauges or ground precipitation radars.

Precipitation exhibits spatial and temporal variability across a wide range of scales ranging from the microscale (sub-kilometric, sub-hourly) to the synoptic and multidecadal scales. This variability includes specific spatio-temporal modes corresponding to regular features which may be periodic such as the diurnal cycle, seasonal cycle, intraseasonal cycles (e.g. due to the Madden-Julian Oscillation), interannual cycles (e.g. due to the El Niño–Southern Oscillation) or potentially long-term trends (e.g. effects of anthropogenic aerosols and greenhouse gas emissions). These regular modes of precipitation variability co-exist and interact with less predictable chaotic

variability, resulting in complex regional and local patterns of precipitation. An important question about satellite QPEs is how well the space-time dynamics of precipitation are captured across a range of scales relevant for hydrologic applications and decision support.

The classical approach for comparing a QPE to a reference measurement is to gather a set of coincident samples, i.e. individual estimates, each one corresponding to a given time and location, and compute sample statistics such as correlations, mean squared differences, detection rate, false alarm rate, etc. With this approach, which focuses on point or “pixel” statistics, each sample is considered independently and the fact that precipitation is a spatially and temporally correlated variable is ignored. As such, the classical scoring metrics do not inform us on the ability of QPE products to accurately capture the spatial and temporal *patterns* of precipitation. The interpretation of point or pixel sample statistics is always ambiguous for spatially and temporally correlated variables and the analysis of the sample statistics gives little insight about the nature of the retrieval errors, which could be additive or multiplicative random noise, but also systematic or random errors on the location and timing of the precipitation features, spatial and temporal distortion of the precipitation features, etc. Finally, from sample statistics computed at one given scale only, one cannot infer the performance of a precipitation product at any other scale. An alternative evaluation approach is object-based analysis, where a continuous precipitation area (above a given threshold) is defined as an object (e.g. Ebert and McBride 2000, Demaria et al. 2011, Tapiador et al. 2019, Li et al. 2020, Ayat et al. 2021). This approach allows to partially circumvent the above-mentioned limitations. However, these types of methods are generally parametric (one important parameter being the intensity threshold chosen to define an object), and the results may be highly sensitive to the definition of the objects. As such, these methods are not easily applicable to large datasets without human supervision, and the results of studies performed

with different parametric and methodological choices are not easily comparable. Additionally, complex mechanisms such as object splitting and merging over time may make the object-related statistics delicate to interpret.

Spectral representations such as the Fourier transform or wavelet transform are designated tools to analyze the dynamics of spatio-temporal variables (Yiou et al 1996, Kyriakidis and Journel 1999, Oreopoulos et al. 2000, Harris et al. 2001, Ghil et al. 2002). In particular, using a multidimensional space-time spectral analysis allows one to consider jointly spatial and temporal dynamics. Unlike the sample statistics, the space-time Fourier spectral analysis provides information on: the size and lifetime of the precipitation systems/features; the potential spatial anisotropy of precipitation fields, including propagation effects with preferred directionality and propagation speed; and statistics on the dynamical modes of variability of precipitation, such as the diurnal and seasonal cycles or the response to atmospheric pressure waves (from small-scale internal gravity waves to synoptic Kelvin and Rossby waves). Fourier space-time spectral analysis has been used in climate science for several decades to identify modes of variability and evaluate model dynamics (Kao and Wendel 1970, Hayashi 1982, Wheeler and Kiladis 1999, Céron and Guérémy 1999, Orbe et al. 2020). It has also been used to investigate dynamical scaling in precipitation (Rysman et al. 2013) and sometimes to parametrize stochastic representations of rainfall (Kundu and Bell 2003, De Michele and Bernardara, 2005). However, it has rarely been used to evaluate and compare observational datasets. The evaluation of the dynamical aspects of precipitation is particularly relevant to multi-satellite QPEs as the spatio-temporal sampling allowed by a constellation of satellites on different orbits is itself highly dynamical, and the interpolation methods used to estimate precipitation between the observations often rely on dynamical constraints.

In the present study, five satellite QPEs, namely CMORPH, GSMaP, IMERG-early, IMERG-final and PERSIANN-CCS (see Section 2 for detailed information and acronyms) are evaluated against NOAA’s gauge-radar Ground Validation Multi-Radar Multi-Sensor (GV-MRMS) product over the southeastern United States at scales down to 10 km and 1 hour through (cross-)spectral space-time analysis relying on a three-dimensional Fast Fourier Transform (FFT). The three dimensions of the analysis are the two spatial dimensions (N-S and E-W directions) and the temporal dimension. The marginal (single-variable) and joint distributions of the spectral power of the precipitation signal as a function of temporal frequency and spatial wavenumbers, revealed by the Power Spectral Density (PSD), allows us to verify the scales at which the products have realistic spatio-temporal dynamics. Additionally, the spectral coherence between the satellite QPEs and the ground reference allows us to determine the scales at which the satellite can accurately reproduce the space-time dynamics of precipitation, as observed by the gauge-radar network, with concordant timing and location of the precipitation features. In Guilloteau et al. (2017) and Guilloteau and Foufoula-Georgiou (2020) the concept of spatial “effective resolution” of a product was introduced based on the spatial wavelet coherence between the evaluated product and reference gauge-radar fields. Here, this concept is extended to the spatial and temporal dimensions simultaneously.

The article is organized as follows. Section 2 presents the datasets, the study area and briefly introduces the spectral analysis method. Section 3 presents a case study of spectral analysis applied to a storm system to gain insight on the interpretation of the proposed metrics. Section 4 presents the results from the analysis of all data over a two-year period as a comparison of the spectral properties of the GV-MRMS reference dataset with those of the satellite QPEs. In Section 5 the spectral performance of an idealized gauge network is presented to quantify the gauge density

necessary to achieve performance similar to the satellite retrievals and thus assess the “equivalent gauge value” of the satellite products. Section 6 presents a discussion on the effect of different retrieval methods and algorithms on the spectral properties of the retrieved precipitation fields. The dilemma of preserving the true space-time power spectrum of precipitation versus minimizing the mean squared retrieval error is discussed in this section. Section 7 presents the concluding remarks.

## **2. Data and methods**

### *a. GV-MRMS gauge-radar data*

The half-hourly gauge-radar QPE from the Ground Validation Multi-Radar Multi-Sensor (GV-MRMS, Petersen et al. 2020) suite of products is used in this study as a high-quality reference to evaluate the satellite QPEs. GV-MRMS builds on the MRMS QPE that is derived from WSR-88D radars and more than 18,000 automatic hourly rain gauges over the contiguous United States and Canada (Zhang et al. 2016). Advanced data integration techniques are used to create 3-D reflectivity mosaic grids and quantitative precipitation estimates blending radar and gauge data at the necessary resolution for the evaluation of satellite QPEs. Less trustworthy GV-MRMS estimates are filtered using a radar quality index and gauge-based quality control. These procedures are necessary to obtain a high-quality and standardized reference across the study domain for satellite evaluation purposes (Kirstetter et al. 2012, 2020). The half-hourly precipitation estimates are produced on a regular grid with 0.01° latitude and longitude increments. The southeastern part of the United States between the latitudes 30 ° and 41° N and longitudes 81° and 102° W (Figure 1), over which the radar coverage is excellent (49 radars cover this 2.3 million

square kilometers area), as well as excellent gauge coverage, is selected as a benchmark area for evaluating the satellite QPEs. We consider here that the errors of the GV-MRMS estimation at the 10 km hourly resolution at which our analysis is performed are negligible compared to the errors in the satellite QPEs. The ability of the gauge-radar product to capture the fine-scale variability of precipitation is trusted in particular because of the high instrumental resolution and sampling frequency of the radars. The GV-MRMS dataset provides the spatial and temporal continuity required to study the spatio-temporal structure of precipitation fields.

#### *b. Multi-satellite precipitation products*

Five multi-satellite precipitation products are evaluated in the present study. All of them are quasi-global products, covering all longitudes and the latitudes between 60°N and 60°S. All five products offer an hourly or higher temporal sampling and provide precipitation estimates on a grid with a latitude/longitude increment equal to or finer than 0.1°. They are all publicly available for research purposes.

The PERSIANN-CCS (Precipitation Estimation from Remotely Sensed Information using Artificial Neural Networks – Cloud Classification System, Hong et al. 2004), derives precipitation estimates from the longwave thermal infrared channel (wavelength between 10 and 12.5μm) of imagers on geostationary orbits. The area considered in this study was monitored by the Advanced Baseline Imager (ABI) onboard the GOES-16 satellite during the 2018-2020 study period. The algorithm first performs a cloud classification based on texture parameters. A relation between the infrared brightness temperature and the precipitation intensity, specific to each cloud class is then used to estimate half-hourly accumulated precipitation. PERSIANN-CCS is produced by the Center for Hydrometeorology and Remote Sensing of the University of California Irvine.

GSMaP-MVK (Global Satellite Mapping of Precipitation - Moving Vector with Kalman filter, Ushio et al. 2009) has been developed by the Japan Aerospace Exploration Agency (JAXA) as part of the Tropical Rainfall Measuring Mission (TRMM; Kummerow et al. 2000) and Global Precipitation Measurement (GPM) mission (Hou et al. 2014) international programs. It relies on the estimation of precipitation rates from about a dozen multispectral microwave imagers and sounders on low earth orbits. To fill the gaps between the satellite overpasses, a dynamic interpolation is performed relying on cloud motion vectors derived from geostationary infrared (Geo-IR) imagery and Kalman filtering. Version 7 of the product is used in the present study.

The CPC Morphing technique (CMORPH, Joyce et al. 2004, Joyce and Xie 2011, Xie et al. 2017) produced by the United States National Oceanic and Atmospheric Administration (NOAA) Climate Prediction Center, is similar in concept to GSMaP. It relies on a similar constellation of microwave imagers and sounders (most of them being common with those used for the GSMaP algorithm), and also implements a Kalman filter interpolation approach with Geo-IR-derived cloud motion vectors. CMORPH and GSMaP differ by the microwave retrieval schemes used for estimating precipitation rates and the parametrization of the Kalman filter. For Version 1.0 of the CMORPH product, used in the present study, the quantitative biases of CMORPH over land are corrected locally with correction parameters estimated from the climatology of the CPC gauge analysis product over 30 calendar-day periods.

The Integrated Multi-satellite Retrievals for GPM (IMERG, Huffman et al. 2019) product has been developed by the United States National Aeronautics and Space Administration (NASA) as part of the GPM international program. It relies on the GPM international constellation of low earth orbit microwave imagers and sounders (Hou et al. 2014) and on Geo-IR. It implements a CMORPH-like motion vector method to dynamically interpolate the microwave-derived

precipitation rates, though in Version 06, used in the present study, the motion vectors are computed from the total precipitable water vapor field of numerical models instead of Geo-IR (Tan et al. 2019). IMERG additionally assimilates the infrared precipitation rates from the PERSIANN-CCS algorithm as part of the Kalman filtering process. Three different IMERG products are made available with different latency: the “early” product (IMERG-E) is available 4 hours after observation times, the “late” (IMERG-L) is available 14 hours after observation and the “final” product (IMERG-F) is available 4 months later. IMERG-E implements a one-way Kalman filter approach while IMERG-L and IMERG-F rely on a two-way Kalman smoother (i.e. dynamical interpolation from both “past” and “future” observations at estimation time). The “late” and “final” products also assimilate a higher number of microwave observations than the “early” product as all microwave observations are not always available with the 4 hours latency. The “uncalibrated” precipitation estimates that do not include gauge adjustment from IMERG-E and IMERG-F products are used in the present study.

The January 2018 to April 2020 period is selected for the evaluation of the satellite products. The March 2018 and March 2019 months are excluded from the analysis because of a high rate of missing MRMS data (or data not meeting the high GV quality standard) for this period. As the Fourier transform does not accommodate discontinuous data in space and time, all gaps in the data must be interpolated; in the present article a linear temporal interpolation is used for missing data when the gap is shorter than two hours. The native space-time grid sampling of CMORPH, GSMaP, IMERG and PERSIANN-CCS are respectively  $0.08^{\circ} \times 0.08^{\circ} \times 30\text{min}$ ,  $0.1^{\circ} \times 0.1^{\circ} \times 60\text{min}$ ,  $0.1^{\circ} \times 0.1^{\circ} \times 30\text{min}$  and  $0.04^{\circ} \times 0.04^{\circ} \times 60\text{min}$ .

*c. Space-time Fourier spectral analysis*

Our space-time spectral analysis relies on a three-dimensional Fourier transform. If  $g(x, y, t)$  is a function of space and time, for example, an estimate of precipitation intensity, its Fourier transform is defined as:

$$\hat{g}(k_x, k_y, f) = \iiint_{-\infty}^{+\infty} g(x, y, t) e^{-i2\pi(k_x x + k_y y + f t)} dx dy dt \quad (1)$$

with  $k_x$  and  $k_y$  the spatial wavenumbers and  $f$  the temporal frequency. The Fourier power spectral density (PSD) of  $g(x, y, t)$  is defined as:

$$P_g(k_x, k_y, f) = \hat{g}(k_x, k_y, f) \times \hat{g}^*(k_x, k_y, f) \quad (2)$$

with the operator  $*$  denoting the complex conjugate. The Fourier power cross-spectral density (PCSD) between two functions  $g(x, y, t)$  and  $h(x, y, t)$ , for example, two different estimates of precipitation intensity, is defined as:

$$P_{gh}(k_x, k_y, f) = \hat{g}(k_x, k_y, f) \hat{h}^*(k_x, k_y, f) \quad (3)$$

In practice, for finite-length datasets, a discrete Fast Fourier Transform (FFT) is used and local averaging in the Fourier frequency-wavenumber domain is necessary to obtain robust estimates of the PSD and PCSD (Proakis, 2001). The PSD reveals how the analyzed signal can be decomposed as a sum of oscillations (waves) and how much energy is associated with these waves as a function of the wavenumber (number of oscillations per unit of space) and the frequency (number of oscillations per unit of time). The PCSD indicates whether the oscillations contained in two different signals synchronize or not and how much common energy they have. We use here the term “energy” in the statistical sense, meaning the integral value over space and time of the square of a variable (here precipitation rate); it is not directly related to the physical energy (in the thermodynamics sense) of the atmospheric systems. Power is defined as energy per unit of

time/space. The space-time PSD and PCSD are uniquely related to the space-time autocorrelation and cross-correlation functions through the Wiener-Khinchin theorem (Cohen, 1998).

The Fourier spectral coherence between  $g(x, y, t)$  and  $h(x, y, t)$  is defined as:

$$C_{gh}(k_x, k_y, f) = \frac{P_{gh}(k_x, k_y, f)}{\sqrt{P_g(k_x, k_y, f) \times P_h(k_x, k_y, f)}} \quad (4)$$

The spectral coherence is a complex number with a modulus between 0 and 1. It can be interpreted as the complex correlation of the Fourier coefficients within narrow frequency/wavenumber bands. The phase (argument) of the spectral coherence gives the average phase shift between the two variables in each frequency/wavenumber band. A null spectral coherence indicates unsynchronized oscillations with a randomly varying instantaneous phase shift between the two signals at the corresponding periods and wavelengths. A spectral coherence with a unit modulus indicates identical oscillating signals (up to a multiplicative constant and a constant phase shift) at the corresponding period and wavelength.

The PSD and the spectral coherence being quadratic measures, they are strongly influenced by the extreme values in the signal. One can analyze the space-time dynamics of precipitation with regard to a specific precipitation intensity value (or a specific quantile) by thresholding the precipitation fields in order to obtain a binary variable before performing the spectral analysis (not done here). Alternatively, one could perform the spectral analysis on the quantile fields, i.e. on the intensity values mapped to a uniform distribution. The classical sample statistics, mean squared difference (MSD) and Pearson correlation coefficient (CC) can be derived from the power spectral and cross-spectral densities:

$$MSD_{gh} = \iiint_{-\infty}^{+\infty} [P_g + P_h - 2 \operatorname{Re}(P_{gh})] dk_x dk_y df$$

(5)

$$CC_{gh} = \iiint_{0^+}^{+\infty} \operatorname{Re}(P_{gh}) dk_x dk_y df \times \left( \iiint_{0^+}^{+\infty} P_g dk_x dk_y df \times \iiint_{0^+}^{+\infty} P_h dk_x dk_y df \right)^{-1/2}$$

(6)

where  $\operatorname{Re}(P_{gh})$  is the real part of  $P_{gh}$ .

Because of the difficulty in visually representing functions of three variables, in the present article, we show the marginal PSDs as well the joint PSDs along two of the three dimensions. The marginal PSD along one dimension is obtained by integrating the three-dimensional PSD along the other two dimensions. Similarly, the joint PSD along two dimensions is obtained by integrating the three-dimensional PSD along the third dimension. In the following, spectral quantities are interpreted as functions of temporal period and spatial wavelengths rather than frequency and wavenumbers; wavelength and period are the inverse of wavenumber and frequency respectively.

Before applying the Fourier transform, the GV-MRMS and satellite QPEs are projected (and interpolated when necessary) on a common  $0.1^\circ \times 0.1^\circ \times 30\text{min}$  latitude/longitude/time grid. The 30 min temporal sampling is used for better spectral resolution but the temporal periods shorter than 2 h are excluded from the analysis after the Fourier transform to avoid penalizing GSMaP and PERSIANN-CCS, which have an hourly native sampling. The spatial wavelengths are shown in km, which is converted from degrees latitude/longitude using the following conversion ratio for

the study region:  $1^\circ$  latitude corresponds to approximately 110 km while  $1^\circ$  longitude corresponds to approximately 90 km.

### 3. A case study for the interpretation of spectral quantities for storm diagnostics

In this section we demonstrate the methodology on a specific storm system to gain physical insight on the results before applying it to an ensemble of storms over a period of two years. Specifically, through the comparison of the satellite and gauge-radar space-time PSDs as well as the analysis of their relative spectral coherence, we evaluate how well satellite-derived products reproduce precipitation features across space-time scales, such as: (1) the *morphology* and *orientation* of the storm system, (2) *the dynamics and propagative features (speed and direction)*, and (3) *consistency of precipitation features' location and timing*.

Since the analysis is performed over a range of scales, we can assess the space-time scales at which precipitation variability is adequately represented in the products (“effective space-time resolution”). In this case study, we perform the space-time spectral analysis of GV-MRMS, IMERG-F and PERSIANN-CSS precipitation fields over the study area for a two-day period (1900 UTC 2 May 2018 to 0800 UTC 4 May 2018) during which a frontal mesoscale convective storm system with several squall lines propagated from west to east (see the evolution of the system as captured by GV-MRMS, IMERG-F and PERSIANN-CCS on Figure 2 and in the animation provided as online supplementary material).

The PSDs resulting from the three-dimensional Fourier transform are shown on Figure 3. We first analyze the joint PSDs along the two spatial dimensions (Figure 3, left column). Passing into the polar coordinate system through the change of variable  $k = \sqrt{k_x^2 + k_y^2}$  and  $\theta =$

304  $\text{atan}(\frac{k_x}{k_y})$ , we can assess the dependence of the PSD on the azimuthal direction  $\theta$ . Here,  $\theta$  is defined  
 305 as the angle clockwise from the North, following the traditional compass convention. For the GV-  
 306 MRMS and the two satellite products, the two-dimensional spatial PSD exhibits a preferred  
 307 directionality, revealing the anisotropy of the precipitation fields. Specifically, the PSD is higher  
 308 in the directions between  $290^\circ$  and  $330^\circ$  than in the other directions; this direction is the direction  
 309 of the strongest gradients in the precipitation, i.e. the direction orthogonal to the squall lines. The  
 310 anisotropy is particularly pronounced for GV-MRMS, for which it affects all wavelengths down  
 311 to the 20 km wavelength. For IMERG-F the anisotropy is strong at long wavelengths but fades  
 312 progressively at wavelengths shorter than 100 km, revealing that IMERG-F only shows  
 313 pronounced directionality for the precipitation features of dimension larger than  $\sim 100$  km. For  
 314 PERSIANN-CCS the anisotropy is only salient at wavelengths longer than 200 km. These  
 315 differences in the PSD are related to the different morphology of the storm across the three  
 316 products (Figure 2). GV-MRMS shows a well-defined frontal system with a narrow convective  
 317 front forming thin lines in the SW to NE direction. While IMERG-F captures well the general  
 318 shape and orientation of the frontal storm system, the convective areas in the IMERG-F fields are  
 319 thicker and less elongated than in the GV-MRMS fields. The general shape of the system is less  
 320 elongated in the PERSIANN-CSS product which tends to produce elliptic precipitation areas with  
 321 relatively low eccentricity.

322 The joint space-time PSDs are only shown for the E-W direction (Figure 3, right column).  
 323 Two-dimensional space-time PSDs are commonly used in climate and Earth science to analyze the  
 324 propagation of atmospheric and oceanic waves along longitudes (Wheeler and Kiladis 1999, Lin  
 325 et al. 2006, Orbe et al. 2020). The left half of the PSD (negative wavelengths) corresponds to  
 326 eastward propagating waves and the right half (positive wavelengths) corresponds to westward

propagating waves. The two-dimensional space-time PSD shows the energy of the eastward and westward propagating waves as a function of their spatial wavelength and temporal period. The ratio between wavelength and period defines the phase propagation velocity of the waves. A linear relationship between wavelength and period indicates non-dispersive wave propagation (i.e. a phase velocity independent of the wavelength). For the present case study, the eastward propagation of the storm system appears neatly in the PSD, with most of the spectral power associated with the negative wavelengths. The propagation speed of the system is also revealed by the space-time PSD, with the spectral power concentrated along the lines corresponding to 40 to 90 km/h velocity. GV-MRMS shows more spectral power than IMERG-F and PERSIANN-CCS at temporal periods shorter than 4 h and wavelengths shorter than 200 km.

The spectral coherence (modulus) between GV-MRMS and the satellite products (Figure 4) allows us to evaluate the ability of IMERG-F and PERSIANN-CCS to capture precipitation features with the right timing and location as functions of spatial wavenumber (wavelength), temporal frequency (period), directionality of the spatial gradients, propagation speed and propagation direction of the features. In this case study, it appears that PERSIANN-CCS only captures accurately the spatial gradients down to the 100 km wavelength and the temporal dynamics down to the 4 h time period, at finer space-time scales, the coherence with GV-MRMS is not statistically significant (at the 0.01 level). IMERG-F captures accurately the gradients down to the 50 km wavelength and the temporal dynamics down to the 2 h time period. The dominant features propagating eastward with a 40 to 90 km/h velocity are the ones for which the spectral coherence with GV-MRMS is the highest for both IMERG-F and PERSIANN-CCS, revealing that the satellite products capture well the dominant propagative features, but not so well the secondary or local propagative patterns.

We note that the total precipitation associated with the storm system presented in this case study is overestimated by a factor of 1.5 in IMERG-F and by a factor of 1.8 in PERSIANN-CCS compared to the GV-MRMS reference estimate, with area-averaged cumulated precipitations of 19 mm, 29 mm and 33 mm for MRMS, IMERG-F and PERSIANN-CCS respectively. However, one should note that constant multiplicative biases do not affect the spectral coherence or the shape of the PSD function. In the present article, all PSDs shown are normalized by the PSDs at the zero frequency and zero wavenumbers, i.e. the power associated with the mean value of the signal (the DC, or “Direct Current”, component in signal processing terminology).

#### **4. Comparison of five multi-satellite products from two years of data**

The performance evaluation consists of the comparison of the PSD of the satellite QPEs with the PSD of GV-MRMS and the analysis of the spectral coherence between the satellite QPEs and GV-MRMS as functions of spatial wavenumber (wavelength), temporal frequency (period), directionality of the spatial gradients, propagation speed and propagation direction of the features. One advantage of the spectral approach, as compared for example to object-based approaches, is that one can compute spectra over a long time period and a large area and extract the average characteristics of storm systems without having to identify each storm individually.

##### *a. Marginal PSDs: spatial and temporal variability assessed independently*

Figure 5 (top) shows the marginal PSDs along time and the two spatial dimensions. All products show a peak corresponding to the diurnal cycle of precipitation at the one-day period and the 0.5 days harmonic (indicating that the diurnal cycle is not perfectly sinusoidal) is also visible in the PERSIANN-CCS spectrum. While the shape and timing of the diurnal cycle varies across

the study region, the PERSIANN family products generally have a pronounced diurnal cycle with a narrow single peak in the afternoon (Dai and Hsu 2007, Nguyen et al. 2020). Beside this peak for the diurnal cycle all spectra show decreasing PSD with shorter periods and wavelengths, reflecting the well-known fact that precipitation is a spatially and temporally correlated variable with correlation decreasing at longer distances and greater temporal delays (Zawadzki 1973, Waymire and Gupta 1981). It is, however, worth noting that neither the temporal power spectra nor the spatial spectra appear linear in the log-log scale. The approximation of the temporal or spatial marginal PSD by a power law of the form  $P(f) = \alpha f^\beta$ , or respectively  $P(k) = \alpha k^\beta$ , (i.e. as a “warm color” power spectrum when  $\beta < 0$ ), which is often found in the literature for climate variables (Gilman et al. 1963, Lovejoy and Schertzer 1986, Harris et al. 2001, Tustison et al. 2001), would therefore be a poor approximation of the empirical PSDs in the present case. The GV-MRMS reference spectrum is the one showing the strongest deviation from log-log linearity for both temporal and spatial spectra.

For the temporal spectra, GV-MRMS and the satellite products show similar distributions of spectral power at periods ranging from 0.5 days to 20 days. For time periods shorter than 0.5 days the satellite products show a significantly faster decay of the PSD with shorter periods than GV-MRMS. This means that the satellite products are temporally smoother, i.e. have higher short-term temporal correlation of the precipitation rates than GV-MRMS. For all products, the spatial spectra in the E-W and N-S directions are nearly identical. All satellite products significantly underestimate the spatial variability at wavelengths shorter than 300 km in both directions when compared to GV-MRMS, indicating excessive short-range spatial correlation in satellite precipitation. We note that the IMERG-E and IMERG-F spatial spectra are nearly identical while

their temporal spectra diverge significantly at periods shorter than 6 h (IMERG-F showing lower PSD than IMERG-E at these high temporal frequencies).

In terms of spectral coherence between the satellite QPEs and GV-MRMS (Figure 5, bottom), all products show a decrease of coherence with shorter periods and wavelengths, with the exception of the peak at the 1-day period. At all temporal periods and at wavelengths longer than 60 km, IMERG-F shows the highest coherence with GV-MRMS, implying that this product is the most consistent with GV-MRMS in terms of coincident spatial and temporal patterns. PERSIANN-CCS shows significantly lower coherence with GV-MRMS than the other satellite products at periods greater than 4 h and at wavelengths longer than 200 km. We note that for wavelengths longer than 50 km CMORPH and IMERG-E show very similar coherence with GV-MRMS. For all satellite products and at all wavelengths, the coherence with GV-MRMS in the N-S and E-W directions is also very similar.

*b. Joint E-W and N-S spatial PSDs: directional morphology of precipitation systems*

We now analyze the PSD as a function of the two E-W and N-S spatial dimensions (Figure 6). The first noticeable characteristic is the circular asymmetry of the PSDs, with higher power density in the 320° azimuthal direction (approximately NW-SE). This reveals the spatial anisotropy of the precipitation fields; the strongest spatial gradients are found around the 320° direction while lower variability (higher spatial correlation) is found in the orthogonal direction (50°, approximately SW-NE). This is consistent with the fact that most of the linear precipitation features such as squall lines are approximately oriented along the SW-NE direction in the southeastern United States (Newton 1950). It is worth noting that, because the preferred direction is neither N-S nor E-W but rather the “diagonal” direction, the anisotropy was not apparent from the marginal N-S and E-W PSDs (Figure 5). This shows that computing the unidimensional spatial

PSD (or variogram / autocovariance function) in only two orthogonal directions is generally not sufficient to detect anisotropy. We note that the small increase of the PSDs in the  $0^\circ$ ,  $90^\circ$  and  $270^\circ$  directions is an artifact caused by the fact that the pixels are  $0.1^\circ \times 0.1^\circ$  squares. All the satellite QPEs reproduce the spatial anisotropy shown by GV-MRMS; we note however that the anisotropy appears less pronounced for PERSIANN-CCS than for the other products. We compute the average PSD as a function of the spatial direction by integrating the two-dimensional spatial PSD between wavelengths 20 km and 300 km for each azimuthal angle  $\theta$  (Figure 8, left panel). From this function  $\text{PSD}(\theta)$  we compute the anisotropy factor, which we define as the ratio between the maximum and the minimum of  $\text{PSD}(\theta)$ . The anisotropy factors for GV-MRMS and each of the satellite products are listed in Table 1. PERSIANN-CCS has a lower anisotropy factor (2.1) than GV-MRMS (2.5) and the other satellite products (2.4 to 2.5). Another quantitative metric shown in Table 1 is the sub-meso power fraction. We also derive this metric from the two-dimensional spatial PSD; it is defined the fraction of the spectral power explained by the wavelengths shorter than 300 km. The sub-meso power fraction is found significantly lower for all the satellite products (45% to 51%) than for GV-MRMS (62%), confirming the fact that the gauge-radar product shows higher fine-scale variability than the satellite products.

Comparing the five satellite products to GV-MRMS to assess how well they reproduce the precipitation spatial organization, with accurate localization of the spatial features, Figure 7 shows the spectral coherence between GV-MRMS and the satellite QPEs as a function of the spatial N-S and E-W wavelengths. Figure 8 (right panel) shows the integrated coherence for wavelengths between 20 km and 300 km as a function of the azimuthal angle. We note that the direction of maximal PSD is also the direction of maximal coherence for all the satellite products, except for PERSIANN-CCS, for which the maximum coherence with GV-MRMS is found in the north ( $0^\circ$ )

direction. Simple signal to noise ratio considerations can explain the fact that the stronger gradients in the SE to NW direction are better captured by the satellites: the higher magnitude of precipitation variability in this direction is expected to cause a higher-magnitude signal in the measured radiances in the same direction; in contrast, the magnitude of the noise in the measured radiances is expected to be the same in all directions. Higher signal to noise ratio, leading to better retrieved precipitation signal, is therefore expected in the direction of the stronger precipitation gradients. One shall note that, for the retrieval of precipitation from passive instruments in orbit, the “noise” is not only instrumental noise, but also variability in the measured radiances coming from physical phenomena concurrent with precipitation (e.g. variations in the surface temperature and emissivity).

#### *c. Joint space-time PSDs: dynamics and propagative features*

Moving into the assessment of precipitation space-time dynamics, the joint PSDs along the temporal dimension and first the E-W, then the N-S spatial directions are examined. Figure 9 shows the joint PSDs along the temporal dimension and the E-W spatial dimension. One immediately notices the asymmetry, with most of the spectral power associated with negative wavelengths, revealing the dominant eastward propagation of the precipitation features as already found for the case study in Figure 3. For GV-MRMS, the spectral power is concentrated around the line corresponding to a ~60 km/h velocity. For CMORPH and GSMaP the spectral energy is concentrated around the 40 to 60 km/h velocity, while for IMERG-E, IMERG-F and PERSIANN-CCS the spectral power appears slightly shifted toward the higher velocities (60 to 90 km/h). From the space-time PSD, we compute the eastward over westward (E/W) power ratio as the ratio between the average spectral power for the negative and positive wavenumbers (Table 1). We exclude the wavelengths longer than 500 km from the computation of the E/W power ratio because

of the relatively poor spectral resolution at low wavenumbers. The E/W power ratio is a simple metric that compares the total energy of the eastward-propagating waves to the total energy of the westward-propagating waves. All products have a E/W power ratio higher than one, confirming the dominant eastward propagation. GV-MRMS has a E/W power ratio of 2.5, PERSIANN-CCS has a E/W power ratio of 1.5 and other satellite products have a E/W power ratio between 2.2 and 3.1. A possible partial explanation for these differences across the products in terms of propagation velocity and in terms of E/W power ratio is the difference in the way they integrate information from infrared cloud top temperature. The dynamics of cloud top temperature do not perfectly reflect the dynamics of precipitation. For example, the cloud top temperature is affected by atmospheric pressure waves which may propagate in a different direction and with a different phase velocity than the motion of the clouds. These pressure waves may propagate upwind or downwind or be stationary; they are also generally dispersive (with a phase velocity changing with wavelength and frequency). Unlike the cloud top temperature, precipitation generally has a weak response to the short-length atmospheric waves. Among the other elements potentially affecting the space-time PSD of satellite products are non-propagating artifacts generated by the microwave sampling scheme or the infrared cloud classification scheme for PERSIANN-CCS and IMERG.

From Figure 10, one can see again that the frequencies and wavenumbers at which the spectral coherence between GV-MRMS and the satellite QPEs is the highest correspond to the frequencies and wavenumbers of maximal PSD. It is worth noting that the PSDs and coherences computed from two years of data provide results consistent with the case study presented in Section 2.4, showing that this case study was in fact representative of the general topology and dynamics of the storm systems in the study area. The joint PSDs along the temporal dimension and the N-S spatial dimension are shown as supplementary Figure S1. The asymmetry is not as pronounced as

for the E-W direction, but one can still notice more power associated with northward-propagating features than with southward propagating features. The northward over southward (N/S) power ratio is found between 1 and 1.4 for the satellite products and 1.5 for GV-MRMS (Table 1). As for the E-W propagation (Figure 10), the dominant propagating features for the N-S propagation are the ones for which the spectral coherence is the highest (Figure S2). The argument of the spectral coherence (i.e. the phase shift) is not shown in the figures because it is not found to be significantly different from zero for any of the products at any wavenumber and any frequency. This indicates that the temporal delays or spatial shifts found between GV-MRMS and the satellite products are random, instead of being systematic.

Figure 11 (top) shows the omnidirectional space-time PSD of the GV-MRMS precipitation fields, obtained by performing circular integrals of the three-dimensional PSD in the  $k_x k_y$ -plane (the omnidirectional spatial wavenumber being defined as  $k = \sqrt{k_x^2 + k_y^2}$ ). Other panels of Figure 11 show the ratio of the satellite omnidirectional space-time PSDs over the omnidirectional space-time PSD of GV-MRMS. Independently of the temporal period, all the satellite products have a deficit of spectral power for wavelengths shorter than 100 or 200 km, consistent with what was shown by the spatial marginal PSD (Figure 6). This deficit of spectral power is particularly pronounced at wavelengths shorter than 200 km and periods shorter than 4 h for GSMaP and PERSIANN-CCS. IMERG-E and IMERG-F omnidirectional space-time PSDs appear highly similar down to the 6 h time period. IMERG-E shows an excess of spectral power relative to GV-MRMS at periods shorter than 6 h and wavelengths longer than 200 km. This indicates the IMERG-E shows excessively rapid changes in large-scale features. This unrealistic statistical property (large-scale features are normally expected to have a high temporal persistence) is likely to reflect retrieval artifacts. GSMaP, and to a lesser extent CMORPH and PERSIANN-CCS, also

show this excess of spectral power at periods shorter than 6 h and wavelengths longer than 200 km. PERSIANN-CCS also shows an excess of spectral power at wavelengths shorter than 30 km, which reflects the existence of sharp transitions (“jumps”) in precipitation intensity between two adjacent pixels. This is likely an artifact coming from the PERSIANN-CCS cloud segmentation and classification scheme. This effect is also visible in a lesser degree in the IMERG products (which assimilate the PERSIANN-CCS estimates).

Figure 12 shows the spectral coherence of the satellite QPEs with GV-MRMS as a function of temporal period and omnidirectional spatial wavelength. For periods longer than 6 h the spectral coherence increases with increasing wavelength. At periods shorter than 6 h, the coherence is maximum for wavelengths between 150 and 300 km. Of all satellite products, IMERG-F appears to have the highest coherence with GV-MRMS at all wavelengths and periods. By setting a criterion of coherence with GV-MRMS higher than  $0.7$  ( $\approx \sqrt{1/2}$ , corresponding to 50% common variance and to a signal to noise ratio of 1:1 or 0 dB in log scale) at the corresponding frequency and wavenumber), we assessed that the best performing multi-satellite product, IMERG-F, resolves well the space-time dynamics of precipitation at spatial wavelengths down to 250 km and time periods down to 4 h, which corresponds to the transition between the meso scale and the sub-meso scale. We note that, with the GPM constellation, for the study area and period, the average interval between two microwave observations is  $\sim 3$  h, which in theory allows one to resolve temporal periods down to  $\sim 6$  h at best (from the Nyquist–Shannon sampling theorem). The ability to resolve finer temporal periods must be attributed to the information provided by the motion vectors and the Geo-IR data.

We note that, for all satellite products, the spectral statistics (both the satellite over gauge-radar PSD ratio in Figure 11 and the spectral coherence with GV-MRMS in Figure 12) do not vary

much with the time period within the 12 hours to 20 days range. This indicates that the spatial patterns of precipitation are not better retrieved at the 10 days aggregated time scale than at the 6 h aggregated time scale (while they are significantly better retrieved at the 6 h time scale than at the 1 h time scale).

## **5. Satellite spectral performances compared to a theoretical gauge network**

An interesting question to ask is “how many raingauges is a satellite product worth?” i.e., what is the ability of the multi-satellite products to capture the space-time dynamics of precipitation as compared to the ability of a gauge network? To provide insight into this question, we simulated the spatial sampling of a theoretical gauge network by subsampling the 1-km half-hourly GV-MRMS precipitation fields and then interpolated the sparse samples. That is, we created fields of “virtual gauges” distributed on an isometric grid with desired gauge spacing. We used block Kriging as the interpolation method with 10 km target resolution. We know a priori from the Nyquist–Shannon sampling theorem that a gauge spacing shorter than  $L/2$  is necessary to resolve the  $L$  wavelength. However, because the variability of precipitation at wavelengths shorter than  $L$  generates aliasing and sampling noise, this condition is generally not sufficient, and, depending on the rate of decrease of the PSD of precipitation with increasing wavelength, higher sampling rate may be necessary to achieve desired signal to noise ratio at wavelength  $L$ . We simulated several gauge networks and found that with an 80 km gauge spacing we obtain simulated retrieval performance similar to the actual performance of the satellite products.

The result of the spectral comparison of the interpolated virtual gauges with 80 km gauge spacing to the original GV-MRMS fields is shown on Figure 13. Because Kriging is a smooth

interpolation, the interpolated fields show a deficit of spectral power at wavelengths shorter than 100 km or 300 km, depending on the temporal period; the spectral coherence with GV-MRMS is also low at these scales. We notice an excess of spectral power at periods shorter than 6 h and wavelengths longer than 150 km in the interpolated precipitation compared to GV-MRMS. This additive signal at large spatial scales and high temporal frequencies corresponds to the sampling noise. The transition between the well-resolved periods and wavelengths (coherence higher than 0.7) and the unresolved ones (coherence close to 0) is found to be sharper for the simulated gauge networks than for the satellite QPEs, presumably because of the regular spatial sampling of the simulated gauge network. In terms of spectral coherence with GV-MRMS, this idealized gauge network with 80 km gauge spacings show performance comparable with the best performing satellite QPE, IMERG-F. In other words, assuming that the results obtained here from two years of data over the southeastern US are reasonable reflections of the products' global performances, over land, IMERG-F is equivalent to a global network of raingauges spaced 80 km apart. We note that this simple setup only accounts for the effect of spatial sampling and ignores all other sources of error in gauge measurements, such as temporal sampling of tipping gauges, shot noise coming from the discrete occurrence of raindrops, wind effects, etc. (Habib et al. 2001, Kostinski et al. 2006, Kochendorfer et al. 2017). The sub-kilometer variability of precipitation is also ignored.

## **6. Discussion: spectral bias, MSE reduction and insights for retrieval algorithms**

The results presented above show that all of the satellite QPEs evaluated have a deficit of spectral power at wavelengths shorter than 200 km, revealing that they are spatially smooth precipitation estimates with excessive short-range spatial correlation. This “spectral bias” can be partially explained by the fact that the products rely on “smooth” mathematical operators designed

to minimize the mean squared error (MSE) or to provide the most likely estimate given the observations. Among the smooth estimation methods are parametric regression and machine learning algorithms with quadratic cost functions, as well as Bayesian minimum MSE, maximum likelihood or maximum a posteriori estimators. These types of methods generally produce spatially and temporally smooth estimates with reduced variance and reduction in extreme values (a simple manifestation of this phenomenon is for example the regression dilution in linear regression, (Spearman 1904). Of the satellite QPEs evaluated in the present article, the CMORPH, GSMaP and IMERG algorithms implement a Kalman filter procedure, which is also a method prone to smoothing. The microwave radiative scheme used in the IMERG algorithm is a Bayesian minimum MSE algorithm (Randel et al. 2020). Smoothing effects also affect multisource merged estimates when the information provided by the different sources is not consistent. The Kriging spatial interpolation method used in this article is also a minimum MSE method, hence the smoothness of the interpolated precipitation fields.

The spectral unbiasing of the satellite products can be achieved by applying a multiplicative correction factor as a function of temporal frequency and spatial wavenumbers in the Fourier domain (to match the PSD of the radar fields). This unbiasing, as it is a linear filtering procedure, would not affect the spectral coherence between the satellite QPEs and the radar reference; however, it would affect the MSE, potentially increasing it, as discussed below. The spectral unbiasing of precipitation in global climate models has been proposed by Pierce et al. (2015), however only for the unidimensional temporal Fourier spectrum. One shall note that independently correcting the marginal spatial and temporal PSDs would not guarantee getting the right spatio-temporal PSD.

Histogram matching, also referred to in the literature as PDF matching (PDF for probability density function), quantile matching or frequency matching, is a popular method for statistically correcting precipitation QPEs. It consists in applying a monotonic correction function to the precipitation rates to impose a PDF. This method allows one to compensate for the lack of variance and underrepresentation of extreme values in smooth QPEs. However, the histogram matching method only constrains the PDF at the “pixel” level; the effect of histogram matching on space-time correlation and PSD is a-priori unknown. In contrast, constraining the space-time PSD allows one to constrain the second-order moment of the PDF (variance) at every spatio-temporal scale. More advanced spectral methods can constrain the multiscale higher-order moments (Harris et al. 2001).

Rather than performing the spectral unbiasing of the satellite QPEs to match the space-time PSD of the radar, one can perform optimal space-time filtering of the satellite QPEs to further minimize the mean squared difference with the radar (Turner et al. 2004, Guilloteau et al. 2018). The effect of the optimal filter is to suppress or reduce the variability in the satellite QPEs at the frequencies and wavenumbers at which the spectral coherence with the radar is low (and if necessary, at the frequencies and wavenumbers at which the PSD is overestimated by the satellites). As a linear filter, the optimal filter does not affect the spectral coherence with the radar. The PSD of the optimally filtered field is:

$$P_{opt}(k_x, k_y, f) = |C(k_x, k_y, f)|^2 P_{rad}(k_x, k_y, f) \quad (7)$$

with  $C(k_x, k_y, f)$  the spectral coherence between the radar and the satellite QPE, and  $P_{rad}(k_x, k_y, f)$  the PSD of the radar field. One shall note that zero spectral bias, i.e.  $P_{sat}(k_x, k_y, f) = P_{rad}(k_x, k_y, f)$ , and minimization of the MSE through space-time filtering

cannot be achieved together when the coherence is different from 1. Indeed, when the coherence is lower than 1, the optimally filtered field is necessarily smoother (with lower PSD) than the radar reference. As already mentioned, the smoothness in QPEs is generally a side effect of quadratic or maximum likelihood optimization procedures. Therefore, spectral unbiasing and histogram matching generally have a negative effect on the MSE and the correlation coefficient when comparing to a reference dataset, as they partially “undo” the work of the optimal operators. For example, with the satellite QPEs used in the present article, spectral unbiasing would amplify QPE’s variability at the high frequencies and wavenumbers, at which the spectral coherence with the radar is found to be low, and therefore lead to higher mean squared difference with the radar. This can be related to the concept of “double penalty”, which is that, in terms of MSE or correlation with a reference dataset, it is more unfavorable to retrieve a feature with the wrong timing/location than to not retrieve the feature at all (Rossa et al. 2008).

This raises an important question for precipitation estimation, which is: when is minimizing the MSE more important than preserving the statistical properties of precipitation fields (in particular the PDF of precipitation rates and the space-time PSD or autocorrelation), and vice versa? A more technical formulation of this question is: what cost function should be minimized by optimization procedures and machine-learning algorithms for precipitation estimation (Ning et al. 2014, Ebtehaj et al 2014, 2015, Wang et al. 2020, Li et al. 2020)? Obviously, the answer mostly depends on the application. However, because MSE and correlation with a reference product are the most commonly used metrics when QPEs are validated and evaluated, product makers may be inclined to favor these over other aspects. Additionally, the reference datasets against which the products are evaluated may themselves also rely on smooth quadratic or maximum likelihood operators (for example Kriging or other smooth interpolation methods). In that case, similarly

smooth precipitation estimates show more favorable statistics when compared to these references. Indeed, the frequency/wavelength dependent biases and the intensity dependent biases (conditional biases, Ciach et al. 2000, Kirstetter et al. 2013) introduced by the optimization procedures in the retrieval algorithms can cause estimates derived from totally independent sources to have mutually correlated errors. A potential solution to achieve simultaneously both objectives of preserving the true PSD of precipitation and minimizing the MSE is to embrace the satellite QPEs' uncertainty through a multiscale probabilistic/ensemble approach, where each individual realization of the ensemble has a realistic space-time PSD and the ensemble mean constitutes the minimal MSE estimate (Bellerby and Sun 2005, Guilloteau et al. 2018). This approach, which consists in generating ensembles constrained by the observations with an underlying stochastic precipitation model, has also been proposed to derive precipitation fields from gauge and radar measurements (Haberlandt and Gattke 2004, Vischel et al. 2009, AghaKouchak et al. 2010).

## **7. Concluding remarks**

The space-time Fourier spectral analysis of five satellite QPEs and of the GV-MRMS gauge-radar product over the southeastern United States reveals high consistency between the GV-MRMS gauge-radar product and the GSMaP, CMORPH and IMERG multi-satellite products, which all rely partially on microwave satellite measurements, down to the 250 km spatial wavelength and the 4 h temporal period. At these relatively coarse scales, the consistency between the PSDs of the satellite and gauge-radar fields indicates statistically similar spatio-temporal dynamics; additionally, the high spectral coherence ( $>0.7$ ) between the satellite products and GV-MRMS indicates agreement in terms of location and timing of the precipitation features. IMERG-F is the product showing the highest spectral coherence with GV-MRMS at all frequencies and

wavenumbers. At shorter periods and wavelengths, all satellite products show a deficit of spectral power (i.e. excessive smoothness) and a low spectral coherence with GV-MRMS. However, consistent patterns in the joint space-time PSDs reveals that they properly characterize the average spatial anisotropy and the dominant propagative features in terms of speed and direction at all scales for the area and period of the study.

Concerning the “early” and “final” versions of the IMERG product, the differences between the two lie essentially in a higher level of noise at large spatial wavelengths and high temporal frequency in IMERG-E. We note that in terms of its spectral characteristics, this noise is somewhat similar to the sampling noise in spatially interpolated precipitation from point measurements. In the end, we find that the better performance of IMERG-F compared to the other products lies essentially in a better ability to resolve spatial wavelengths greater than 200 km. Resolving the sub-mesoscale dynamics of precipitation from passive satellite instruments and the existing constellation of satellites remains an ongoing challenge.

The performance metrics given in the present article are bulk statistics computed from more than two years of data and over more than 2 million square kilometers area in the southeastern US. In general, the retrieval performances of satellite products are expected to vary with time and location. For example, retrieval performances are known to be dependent on the type of precipitation system (such as convective and stratiform precipitation). However, the multiscale nature of the present analysis does not allow us to separate precipitation types, since, at any scale, every observed scene contains a mixture of different precipitation types. Another factor of performance variability for satellite products relying on several low-orbit instruments is the instantaneous configuration of the constellation. Indeed, the scenes directly sampled by one or several microwave imagers are likely better resolved than the scenes for which the estimates rely

on dynamical interpolation and motion vectors. Recent studies (Tan et al. 2020, Rajagopal et al. 2021) have identified in IMERG data a dependence of the precipitation statistics on the delay between the retrieval time and the actual time of the closest microwave observation at given point. One should note that the orbits of the different microwave radiometers of the constellation on which the CMORPH, GSMaP, and IMERG products rely are not synchronized, and therefore the temporal sampling at a given point is irregular. The Kalman filters in CMORPH, GSMaP, and IMERG are expected to cause more pronounced space-time smoothing when few microwave observations are available within a given time frame. Ongoing developments for future versions of the IMERG algorithm include the SHARPEN method (Tan et al. 2020), designed to compensate for the statistical smoothing resulting from the Kalman filtering through a local histogram matching approach.

The elements mentioned in the discussion about the spectral bias, which reflects the statistical smoothness of precipitation estimates, and its relation to the algorithmic optimization procedures (Section 4) are valid for any retrieved spatio-temporal variable. However, the relatively large uncertainties that exist in the measurement and prediction of precipitation at the sub-mesoscale, and the importance of precipitation extreme statistics in hydrology, climate science and risk management make them particularly relevant in the case of precipitation. Space-time filtering as post-processing to enhance fine-scale variability is a potential solution to correct for the smoothness of satellite precipitation products.

**Acknowledgements:**

The authors acknowledge support provided by NASA's Global Precipitation Measurement program (grant 80NSSC19K0684), and by the National Science Foundation (NSF) under the EAGER program (grant ECCS-1839441) and the TRIPODS+X program (grant DMS-1839336). The support by NASA (grant 80NSSC19K0726) and NSF (grant EAR-1928724) for the organization of the 12th International Precipitation Conference (IPC12) and production of the IPC12 AMS special collection of papers is gratefully acknowledged.

#### **Data availability:**

Part of the GV-MRMS data used in this study is available at <http://dx.doi.org/10.5067/GPMGV/MRMS/DATA101>. The satellite products are publicly available: CMOPRH at <https://doi.org/10.25921/w9va-q159>; GSMAP at <https://sharaku.eorc.jaxa.jp/GSMaP>; PERSIANN-CCS at <https://chrsdata.eng.uci.edu>; IMERG-E at <https://doi.org/10.5067/GPM/IMERG/3B-HH-E/06>; and IMERG-F at <https://doi.org/10.5067/GPM/IMERG/3B-HH/06>.

## References:

- AghaKouchak, A., Bárdossy, A. and Habib, E., 2010: Conditional simulation of remotely sensed rainfall data using a non-Gaussian v-transformed copula. *Advances in water resources*, **33**(6), 624-634, doi:10.1016/j.advwatres.2010.02.010.
- Ayat, H., Evans, J.P., Sherwood, S. and Behrangi, A., 2021: Are storm characteristics the same when viewed using merged surface radars or a merged satellite product?. *Journal of Hydrometeorology*, **22**(1), 43-62, doi:10.1175/JHM-D-20-0187.1.
- Beck, H.E. and Coauthors, 2019: Daily evaluation of 26 precipitation datasets using Stage-IV gauge-radar data for the CONUS. *Hydrology and Earth System Sciences*, **23**(1), 207-224, doi:10.5194/hess-23-207-2019.
- Bellerby, T.J. and Sun, J., 2005: Probabilistic and ensemble representations of the uncertainty in an IR/microwave satellite precipitation product. *Journal of Hydrometeorology*, **6**(6), 1032-1044, doi:10.1175/JHM454.1.
- Casse, C. and Gosset, M., 2015: Analysis of hydrological changes and flood increase in Niamey based on the PERSIANN-CDR satellite rainfall estimate and hydrological simulations over the 1983–2013 period. *Proceedings of the International Association of Hydrological Sciences*, **370**, 117-123, doi:10.5194/piahs-370-117-2015.
- Céron, J. P. and Guérémy, J. F., 1999: Validation of the space–time variability of African easterly waves simulated by the CNRM GCM. *Journal of climate*, **12**(9), 2831-2855, doi:10.1175/1520-0442(1999)012<2831:VOTSTV>2.0.CO;2.

745 Ciach, G.J., Morrissey, M.L. and Krajewski, W.F., 2000: Conditional bias in radar rainfall  
746 estimation. *Journal of Applied Meteorology and Climatology*, **39**(11), 1941-1946,  
747 doi:10.1175/1520-0450(2000)039<1941:CBIRRE>2.0.CO;2.

748 Cohen, L., 1998: The generalization of the Wiener-Khinchin theorem. *Proceedings of the 1998*  
749 *IEEE International Conference on Acoustics, Speech and Signal Processing*, **3**, 1577-1580,  
750 doi:10.1109/ICASSP.1998.681753.

751 Dai, A., Lin, X. and Hsu, K.L., 2007: The frequency, intensity, and diurnal cycle of precipitation  
752 in surface and satellite observations over low-and mid-latitudes. *Climate dynamics*, **29**(7-8), 727-  
753 744, doi:10.1007/s00382-007-0260-y.

754 Demaria, E.M.C., Rodriguez, D.A., Ebert, E.E., Salio, P., Su, F. and Valdes, J.B., 2011:  
755 Evaluation of mesoscale convective systems in South America using multiple satellite products  
756 and an object-based approach. *Journal of Geophysical Research: Atmospheres*, **116**(D8),  
757 10.1029/2010JD015157.

758 De Michele, C. and Bernardara, P., 2005: Spectral analysis and modeling of space-time rainfall  
759 fields. *Atmospheric Research*, **77**(1-4), 124-136, 10.1016/j.atmosres.2004.10.031.

760 Derin, Y. and Coauthors, 2016: Multiregional satellite precipitation products evaluation over  
761 complex terrain. *Journal of Hydrometeorology*, **17**(6), 1817-1836, doi:10.1175/JHM-D-15-  
762 0197.1.

763 Ebert, E.E. and McBride, J.L., 2000: Verification of precipitation in weather systems:  
764 Determination of systematic errors. *Journal of hydrology*, **239**(1-4), 179-202, doi:  
765 10.1016/S0022-1694(00)00343-7.

766 Ebtehaj, A.M., Zupanski, M., Lerman, G. and Foufoula-Georgiou, E., 2014: Variational data  
 767 assimilation via sparse regularisation. *Tellus A: Dynamic Meteorology and Oceanography*,  
 768 **66**(1), 21789, doi:10.3402/tellusa.v66.21789.

769 Ebtehaj, A.M., Bras, R.L. and Foufoula-Georgiou, E., 2015: Shrunk locally linear embedding  
 770 for passive microwave retrieval of precipitation. *IEEE Transactions on Geoscience and remote*  
 771 *sensing*, **53**(7), 3720-3736, doi:10.1109/TGRS.2014.2382436.

772 Ghil, M. and Coauthors, 2002: Advanced spectral methods for climatic time series. *Reviews of*  
 773 *geophysics*, **40**(1), 1:41, doi:10.1029/2000RG000092.

774 Gilman, D.L., Fuglister, F.J. and Mitchell Jr, J.M., 1963: On the power spectrum of “red noise”.  
 775 *Journal of the Atmospheric Sciences*, **20**(2), 182-184.

776 Guilloteau, C., Gosset, M., Vignolles, C., Alcoba, M., Turre, Y.M. and Lacaux, J.P., 2014:  
 777 Impacts of satellite-based rainfall products on predicting spatial patterns of Rift Valley fever  
 778 vectors. *Journal of Hydrometeorology*, **15**(4), 1624-1635, doi:10.1175/JHM-D-13-0134.1.

779 Guilloteau, C., Foufoula-Georgiou, E. and Kummerow, C.D., 2017: Global multiscale evaluation  
 780 of satellite passive microwave retrieval of precipitation during the TRMM and GPM eras:  
 781 Effective resolution and regional diagnostics for future algorithm development. *Journal of*  
 782 *Hydrometeorology*, **18**(11), 3051-3070, doi:10.1175/JHM-D-17-0087.1.

783 Guilloteau, C., Roca, R., Gosset, M. and Venugopal, V., 2018: Stochastic generation of  
 784 precipitation fraction at high resolution with a multiscale constraint from satellite observations.  
 785 *Quarterly Journal of the Royal Meteorological Society*, **144**, 176-190, doi:10.1002/qj.3314.

786 Guilloteau, C. and Foufoula-Georgiou, E., 2020: Multiscale Evaluation of Satellite Precipitation  
787 Products: Effective Resolution of IMERG. In *Satellite Precipitation Measurement*, Springer,  
788 533-558, doi:10.1007/978-3-030-35798-6\_5.

789 Haberlandt, U. and Gattke, C., 2004: Spatial interpolation vs. simulation of precipitation for  
790 rainfall-runoff modelling—a case study in the Lippe river basin. In *Hydrology: Science and*  
791 *practice for the 21st century, Proceedings of the British Hydrological Society International*  
792 *Conference*, **1**, 120-127.

793 Habib, E., Krajewski, W.F. and Kruger, A., 2001: Sampling errors of tipping-bucket rain gauge  
794 measurements. *Journal of Hydrologic Engineering*, **6**(2), 159-166, doi:10.1061/(ASCE)1084-  
795 0699(2001)6:2(159).

796 Harris, D., Foufoula-Georgiou, E., Droegemeier, K.K. and Levit, J.J., 2001: Multiscale statistical  
797 properties of a high-resolution precipitation forecast. *Journal of Hydrometeorology*, **2**(4), 406-  
798 418, doi:10.1175/1525-7541(2001)002<0406:MSPOAH>2.0.CO;2.

799 Hayashi, Y., 1982: Space-time spectral analysis and its applications to atmospheric waves.  
800 *Journal of the Meteorological Society of Japan.*, **60**(1), 156-171,  
801 doi:10.2151/jmsj1965.60.1\_156.

802 Hilker, T. and Coauthors, 2014: Vegetation dynamics and rainfall sensitivity of the Amazon.  
803 *Proceedings of the National Academy of Sciences*, **111**(45), 16041-16046,  
804 doi:10.1073/pnas.1404870111.

805 Hong, Y., Hsu, K.L., Sorooshian, S. and Gao, X., 2004: Precipitation estimation from remotely  
806 sensed imagery using an artificial neural network cloud classification system. *Journal of Applied*  
807 *Meteorology*, **43**(12), 1834-1853, doi:10.1175/JAM2173.1.

808 Hou, A.Y. and Coauthors, 2014: The global precipitation measurement mission. *Bulletin of the*  
809 *American Meteorological Society*, **95**(5), 701-722, doi:10.1175/BAMS-D-13-00164.1.

810 Huffman, G. J. and Coauthors, 2019: NASA global precipitation measurement (GPM) integrated  
811 multi-satellite retrievals for GPM (IMERG). Algorithm theoretical basis document version 06.  
812 [https://gpm.nasa.gov/sites/default/files/2019-05/IMERG\\_ATBD\\_V06.pdf](https://gpm.nasa.gov/sites/default/files/2019-05/IMERG_ATBD_V06.pdf).

813 Joyce, R.J., Janowiak, J.E., Arkin, P.A. and Xie, P., 2004: CMORPH: A method that produces  
814 global precipitation estimates from passive microwave and infrared data at high spatial and  
815 temporal resolution. *Journal of hydrometeorology*, **5**(3), 487-503, doi:10.1175/1525-  
816 7541(2004)005<0487:CAMTPG>2.0.CO;2.

817 Joyce, R.J. and Xie, P., 2011: Kalman filter–based CMORPH. *Journal of Hydrometeorology*,  
818 **12**(6), 1547-1563, doi:10.1175/JHM-D-11-022.1.

819 Kao, S.K. and Wendell, L.L., 1970: The kinetic energy of the large-scale atmospheric motion in  
820 wavenumber-frequency space: I. Northern hemisphere. *Journal of the Atmospheric Sciences*,  
821 **27**(3), 359-375, doi:10.1175/1520-0469(1970)027<0359:TKEOTL>2.0.CO;2.

822 Kerns, B.W. and Chen, S.S., 2020: A 20-Year Climatology of Madden-Julian Oscillation  
823 Convection: Large-Scale Precipitation Tracking From TRMM-GPM Rainfall. *Journal of*  
824 *Geophysical Research: Atmospheres*, **125**(7), doi:10.1029/2019JD032142.

825 Kirschbaum, D.B. and Coauthors, 2017: NASA’s remotely sensed precipitation: A reservoir for  
826 applications users. *Bulletin of the American Meteorological Society*, **98**(6), 1169-1184,  
827 doi:10.1175/BAMS-D-15-00296.1.

828 Kirschbaum, D. and Stanley, T., 2018: Satellite-based assessment of rainfall-triggered landslide  
829 hazard for situational awareness. *Earth's future*, **6**(3), 505-523, doi:10.1002/2017EF000715.

830 Kirstetter, P. E. and Coauthors, 2012: Toward a framework for systematic error modeling of  
831 spaceborne precipitation radar with NOAA/NSSL ground radar-based national mosaic QPE.  
832 *Journal of Hydrometeorology*, **13**(4), 1285-1300, doi:10.1175/JHM-D-11-0139.1

833 Kirstetter, P.E., Viltard, N. and Gosset, M., 2013: An error model for instantaneous satellite  
834 rainfall estimates: evaluation of BRAIN-TMI over West Africa. *Quarterly Journal of the Royal  
835 Meteorological Society*, **139**(673), 894-911, doi:10.1002/qj.1964.

836 Kirstetter, P.-E., W. A. Petersen, C. D. Kummerow, D. B. Wolff, 2020: Integrated multi-satellite  
837 evaluation for the Global Precipitation Measurement mission: Impact of precipitation types on  
838 spaceborne precipitation estimation. In *Satellite Precipitation Measurement*, 583-608, doi:  
839 10.1007/978-3-030-35798-6\_7.

840 Kochendorfer, J. and Coauthors, 2017: The quantification and correction of wind-induced  
841 precipitation measurement errors. *Hydrology and Earth System Sciences*, **21**(4), 1973-1989,  
842 doi:10.5194/hess-21-1973-2017.

843 Kostinski, A.B., Larsen, M.L. and Jameson, A.R., 2006: The texture of rain: Exploring stochastic  
844 micro-structure at small scales. *Journal of Hydrology*, **328**(1-2), 38-45,  
845 doi:10.1016/j.jhydrol.2005.11.035.

846 Kummerow, C. and Coauthors, 2000: The status of the Tropical Rainfall Measuring Mission  
847 (TRMM) after two years in orbit. *Journal of applied meteorology*, **39**(12), 1965-1982,  
848 doi:10.1175/1520-0450(2001)040<1965:TSOTTR>2.0.CO;2.

849 Kundu, P.K. and Bell, T.L., 2003: A stochastic model of space-time variability of mesoscale  
850 rainfall: Statistics of spatial averages. *Water resources research*, **39**(12),  
851 doi:10.1029/2002WR001802.

852 Kyriakidis, P.C. and Journel, A.G., 1999: Geostatistical space–time models: a review.  
853 *Mathematical geology*, **31**(6), 651-684.

854 Li, Z., Wen, Y., Schreier, M., Behrangi, A., Hong, Y. and Lambriksen, B., 2020: Advancing  
855 Satellite Precipitation Retrievals with Data Driven Approaches: Is black box model explainable?.  
856 *Earth and Space Science*, doi:10.1029/2020EA001423.

857 Li, Z., Wright, D.B., Zhang, S.Q., Kirschbaum, D.B. and Hartke, S.H., 2020: Object-Based  
858 Comparison of Data-Driven and Physics-Driven Satellite Estimates of Extreme Rainfall. *Journal*  
859 *of Hydrometeorology*, **21**(12), 2759-2776, doi:10.1175/JHM-D-20-0041.1.

860 Lin, J.L. and Coauthors, 2006: Tropical intraseasonal variability in 14 IPCC AR4 climate  
861 models. Part I: Convective signals. *Journal of climate*, **19**(12), 2665-2690,  
862 doi:10.1175/JCLI3735.1.

863 Lovejoy, S. and Schertzer, D., 1986: Scale invariance, symmetries, fractals, and stochastic  
864 simulations of atmospheric phenomena. *Bulletin of the American meteorological society*, **67**(1),  
865 21-32, doi:10.1175/1520-0477(1986)067<0021:SISFAS>2.0.CO;2.

866 Mehta, A.V. and Yang, S., 2008: Precipitation climatology over Mediterranean Basin from ten  
867 years of TRMM measurements. *Advances in Geosciences*, **17**, 87-91, doi:10.5194/adgeo-17-87-  
868 2008.

869 Newton, C.W., 1950: Structure and mechanism of the prefrontal squall line. *Journal of*  
870 *Atmospheric Sciences*, **7**(3), 210-222.

871 Nguyen, P., Ombadi, M., Gorrooh, V.A., Shearer, E.J., Sadeghi, M., Sorooshian, S., Hsu, K.,  
872 Bolvin, D. and Ralph, M.F., 2020: PERSIANN Dynamic Infrared–Rain Rate (PDIR-Now): A  
873 Near-Real-Time, Quasi-Global Satellite Precipitation Dataset. *Journal of Hydrometeorology*,  
874 **21**(12), 2893-2906, doi:10.1175/JHM-D-20-0177.1.

875 Ning, L., Carli, F.P., Ebtehaj, A.M., Foufoula-Georgiou, E. and Georgiou, T.T., 2014: Coping  
876 with model error in variational data assimilation using optimal mass transport. *Water Resources*  
877 *Research*, **50**(7), 5817-5830, doi:10.1002/2013WR014966.

878 Orbe, C. and Coauthors, 2020: Representation of Modes of Variability in Six US Climate  
879 Models. *Journal of Climate*, **33**(17), 7591-7617, doi:10.1175/JCLI-D-19-0956.1.

880 Oreopoulos, L., Marshak, A., Cahalan, R.F. and Wen, G., 2000: Cloud three-dimensional effects  
881 evidenced in Landsat spatial power spectra and autocorrelation functions. *Journal of*  
882 *Geophysical Research: Atmospheres*, **105**(D11), 14777-14788, doi:10.1029/2000JD900153.

883 Petersen, W.A., Kirstetter, P.E., Wang, J., Wolff, D.B. and Tokay, A., 2020: The GPM Ground  
884 Validation Program. In *Satellite Precipitation Measurement*, Springer, 471-502,  
885 doi:10.1007/978-3-030-35798-6\_2.

886 Pierce, D.W., Cayan, D.R., Maurer, E.P., Abatzoglou, J.T. and Hegewisch, K.C., 2015:  
887 Improved bias correction techniques for hydrological simulations of climate change. *Journal of*  
888 *Hydrometeorology*, **16**(6), 2421-2442, doi:10.1175/JHM-D-14-0236.1.

889 Proakis, J. G., 2001: Nonparametric methods for power spectrum estimation. In *Digital Signal*  
890 *Processing: Principles, Algorithms and Applications*, Pearson Education India, 908-919.

891 Rajagopal, M., Zipser, E., Huffman G. and Russell, J., 2021: Comparisons of IMERG Version 6  
892 Precipitation At and Between Passive Microwave Overpasses in the Tropics. Accepted for  
893 publication in *Journal of Hydrometeorology*.

894 Randel, D.L., Kummerow, C.D. and Ringerud, S., 2020: The Goddard Profiling (GPROF)  
895 Precipitation Retrieval Algorithm. In *Satellite precipitation measurement*, Springer, 141-152,  
896 doi:10.1007/978-3-030-24568-9\_8.

897 Roca, R., Aublanc, J., Chambon, P., Fiolleau, T. and Viltard, N., 2014: Robust observational  
898 quantification of the contribution of mesoscale convective systems to rainfall in the tropics.  
899 *Journal of Climate*, **27**(13), 4952-4958, doi:10.1175/JCLI-D-13-00628.1.

900 Rossa, A., Nurmi, P. and Ebert, E., 2008: Overview of methods for the verification of  
901 quantitative precipitation forecasts. In *Precipitation: Advances in measurement, estimation and*  
902 *prediction*, Springer, 419-452.

903 Rysman, J.F., Verrier, S., Lemaître, Y. and Moreau, E., 2013: Space-time variability of the  
904 rainfall over the western Mediterranean region: A statistical analysis. *Journal of Geophysical*  
905 *Research: Atmospheres*, **118**(15), 8448-8459, 10.1002/jgrd.50656.

906 Sapiano, M.R.P. and Arkin, P.A., 2009: An intercomparison and validation of high-resolution  
907 satellite precipitation estimates with 3-hourly gauge data. *Journal of Hydrometeorology*, **10**(1),  
908 149-166, doi:10.1175/2008JHM1052.1.

909 Spearman, C., 1904: The proof and measurement of association between two things. *American*  
910 *Journal of Psychology*, **15**(1), 72-101.

911 Suepa, T., Qi, J., Lawawirojwong, S. and Messina, J.P., 2016: Understanding spatio-temporal  
912 variation of vegetation phenology and rainfall seasonality in the monsoon Southeast Asia.  
913 *Environmental research*, **147**, 621-629, doi:10.1016/j.envres.2016.02.005.

914 Tan, J., Huffman, G.J., Bolvin, D.T. and Nelkin, E.J., 2019: IMERG V06: Changes to the  
915 morphing algorithm. *Journal of Atmospheric and Oceanic Technology*, **36**(12), 2471-2482,  
916 doi:10.1175/JTECH-D-19-0114.1.

917 Tan, J., Huffman, G.J., Bolvin, D.T., Nelkin, E.J. and Rajagopal, M., 2020: SHARPEN: A  
918 Scheme to Restore the Distribution of Averaged Precipitation Fields. *Journal of*  
919 *Hydrometeorology*, doi:10.1175/JHM-D-20-0225.1.

920 Tapiador, F.J., Marcos, C. and Sancho, J.M., 2019: The convective rainfall rate from cloud  
921 physical properties algorithm for meteosat second-generation satellites: Microphysical basis and  
922 intercomparisons using an object-based method. *Remote Sensing*, **11**(5), 527,  
923 doi:10.3390/rs11050527.

924 Turner, B.J., Zawadzki, I. and Germann, U., 2004: Predictability of precipitation from  
925 continental radar images. Part III: Operational nowcasting implementation (MAPLE). *Journal of*  
926 *Applied Meteorology and Climatology*, **43**(2), 231-248, doi:10.1175/1520-  
927 0450(2004)043<0231:POPFCR>2.0.CO;2.

928 Tustison, B., Harris, D. and Foufoula-Georgiou, E., 2001: Scale issues in verification of  
929 precipitation forecasts. *Journal of Geophysical Research: Atmospheres*, **106**(D11), 11775-11784,  
930 doi:10.1029/2001JD900066.

931 Ushio, T. and Coauthors, 2009: A Kalman filter approach to the Global Satellite Mapping of  
 932 Precipitation (GSMaP) from combined passive microwave and infrared radiometric data. *Journal*  
 933 *of the Meteorological Society of Japan*, **87**, 137-151, doi:10.2151/jmsj.87A.137.

934 Vischel, T., Lebel, T., Massuel, S. and Cappelaere, B., 2009: Conditional simulation schemes of  
 935 rain fields and their application to rainfall–runoff modeling studies in the Sahel. *Journal of*  
 936 *Hydrology*, **375**(1-2), 273-286, doi:10.1016/j.jhydrol.2009.02.028.

937 Wang, G., Han, W. and Lu, S., 2020: Precipitation retrieval by the L1-norm regularization:  
 938 typhoon Hagibis case. *Quarterly Journal of the Royal Meteorological Society*,  
 939 doi:10.1002/qj.3945.

940 Waymire, E.D. and Gupta, V.K., 1981: The mathematical structure of rainfall representations: 1.  
 941 A review of the stochastic rainfall models. *Water resources research*, **17**(5), 1261-1272.

942 Wheeler, M. and Kiladis, G.N., 1999: Convectively coupled equatorial waves: Analysis of  
 943 clouds and temperature in the wavenumber–frequency domain. *Journal of the Atmospheric*  
 944 *Sciences*, **56**(3), 374-399, doi:10.1175/1520-0469(1999)056<0374:CCEWAO>2.0.CO;2.

945 Xie, P., Joyce, R., Wu, S., Yoo, S.H., Yarosh, Y., Sun, F. and Lin, R., 2017: Reprocessed, bias-  
 946 corrected CMORPH global high-resolution precipitation estimates from 1998. *Journal of*  
 947 *Hydrometeorology*, **18**(6), 1617-1641, doi:10.1175/JHM-D-16-0168.1.

948 Yiou, P., Baert, E. and Loutre, M.F., 1996: Spectral analysis of climate data. *Surveys in*  
 949 *Geophysics*, **17**(6), 619-663.

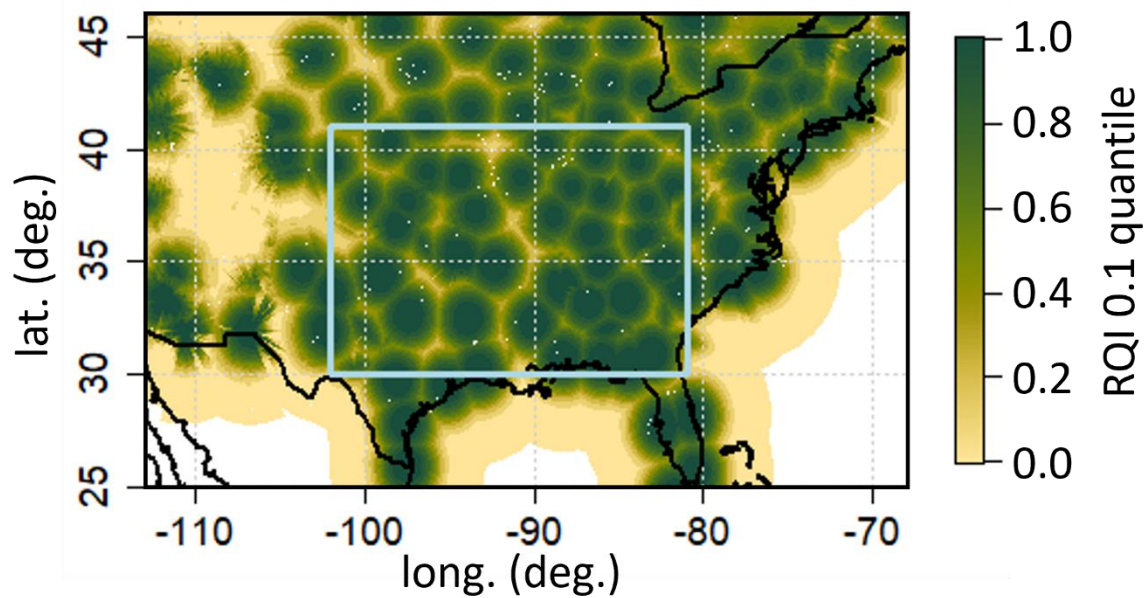
950 Zawadzki, I.I., 1973: Statistical properties of precipitation patterns. *Journal of Applied*  
 951 *Meteorology and Climatology*, **12**(3), 459-472.

952 Zhang, J. and Coauthors, 2016: Multi-Radar Multi-Sensor (MRMS) quantitative precipitation  
953 estimation: Initial operating capabilities. *Bulletin of the American Meteorological Society*, **97**(4),  
954 621-638, doi:10.1175/BAMS-D-14-00174.1.

Product	anisotropy factor	sub-meso power fraction	E/W power ratio	N/S power ratio
MRMS	2.5	62%	2.5	1.5
IMERG-E	2.5	47%	2.7	1.1
IMERG-F	2.4	47%	2.9	1
GSMaP	2.4	51%	2.2	1.4
CMORPH	2.5	45%	3.1	1.2
PERSIANN-CCS	2.1	45%	1.5	1.2

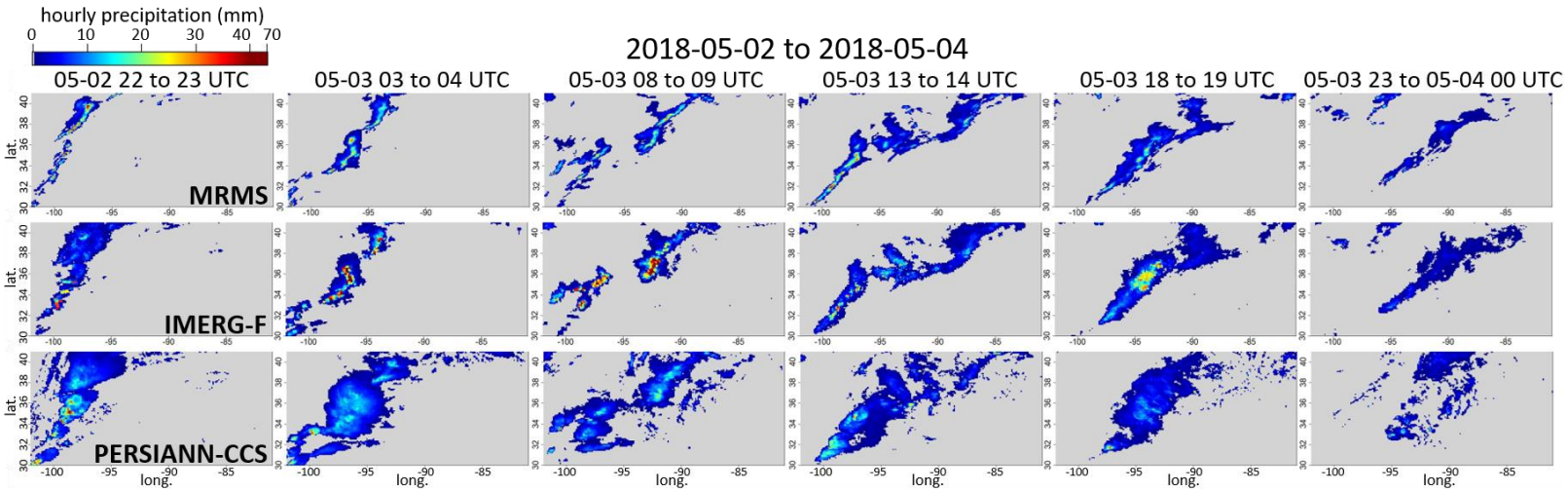
955

956 **Table 1: Storm morphology and space-time dynamics spectral statistics for MRMS and the**  
957 **five satellite products over the southeastern US for the 2018-2020 period.** The anisotropy  
958 factor is defined as the ratio of the maximum over the minimum of the  $PSD(\theta)$  function where  $\theta$   
959 is the azimuthal direction (see Figure 8). The sub-meso power fraction is defined as the fraction of  
960 spectral power associated with wavelengths shorter than 300 km. The eastward over westward and  
961 northward over southward power ratios are derived from the joint space-time PSDs (Figures 9 and  
962 11) by integrating the PSDs over the negative and positive wavenumbers respectively (between  
963 the absolute wavelengths 20 km and 500 km) and computing their ratio.



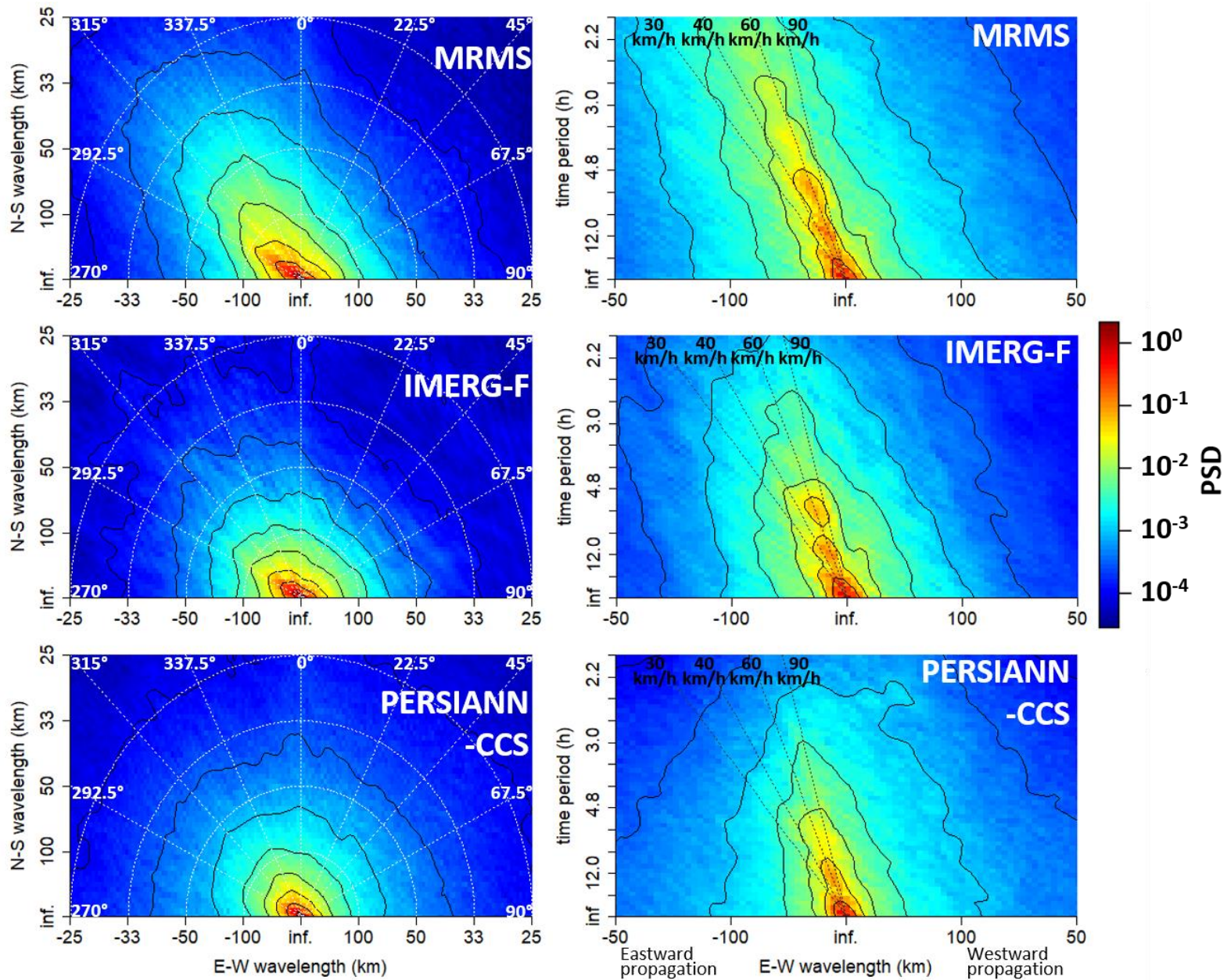
964

965 **Figure 1: Map of the 0.1 lower quantile of MRMS radar quality index over the contiguous**  
 966 **United States.** The blue rectangle corresponds to the study area. The quality index takes into  
 967 account the distance to the closest radar, the altitude of the freezing level and beam blockage by  
 968 the relief (see Zhang et al. 2016 for precise definition). We show here the 0.1 lower quantile,  
 969 meaning that the quality index is higher than the shown value 90% of the time.



970

971 **Figure 2: A case study storm system, as retrieved on 2 May 2018 to 4 May 2018 by GV-**  
 972 **MRMS, IMERG-F and PERSIANN-CCS over the southeastern US.** The images correspond  
 973 to discontinuous snapshots of hourly-accumulated precipitation. An animated version of this figure  
 974 is provided as online supplementary material. The estimates of the area-averaged cumulated  
 975 precipitations for this storm are 19 mm, 29 mm and 33 mm for MRMS, IMERG-F and  
 976 PERSIANN-CCS respectively.



977

978 **Figure 3: Morphology and dynamics of the storm system in Figure 2 as revealed by the PSD.**

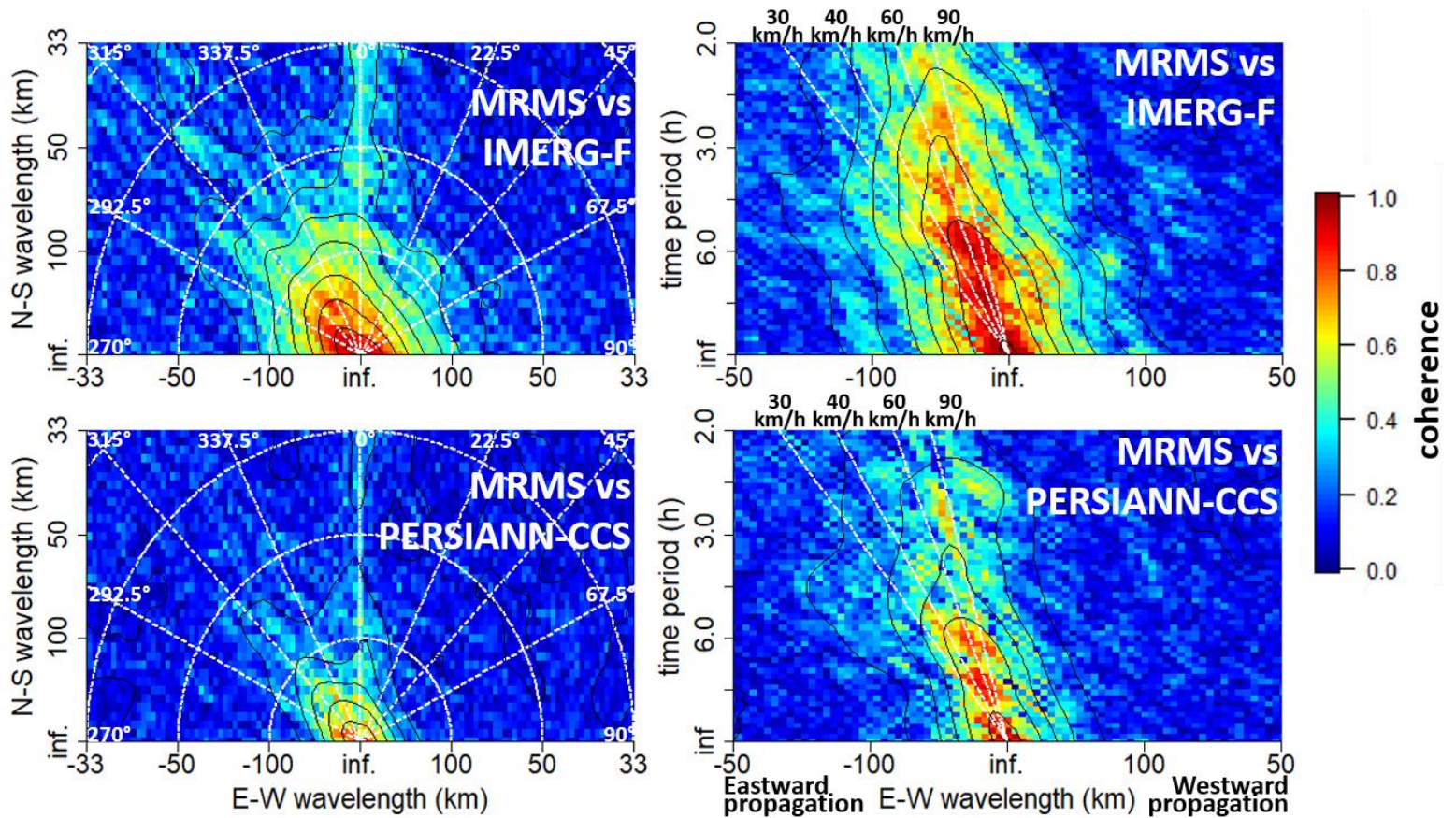
979 (left) Joint PSDs of GV-MRMS, IMERG and PERSIANN-CCS computed over the southeastern

980 US from 1900 UTC 2 May 2018 to 0800 UTC 4 May 2018 along the E-W and N-S spatial

981 dimensions, and (right) along the E-W spatial dimension and the temporal dimension. In the left

982 panels, higher spectral power is found in the 290° to 330° direction (NW), which is the direction

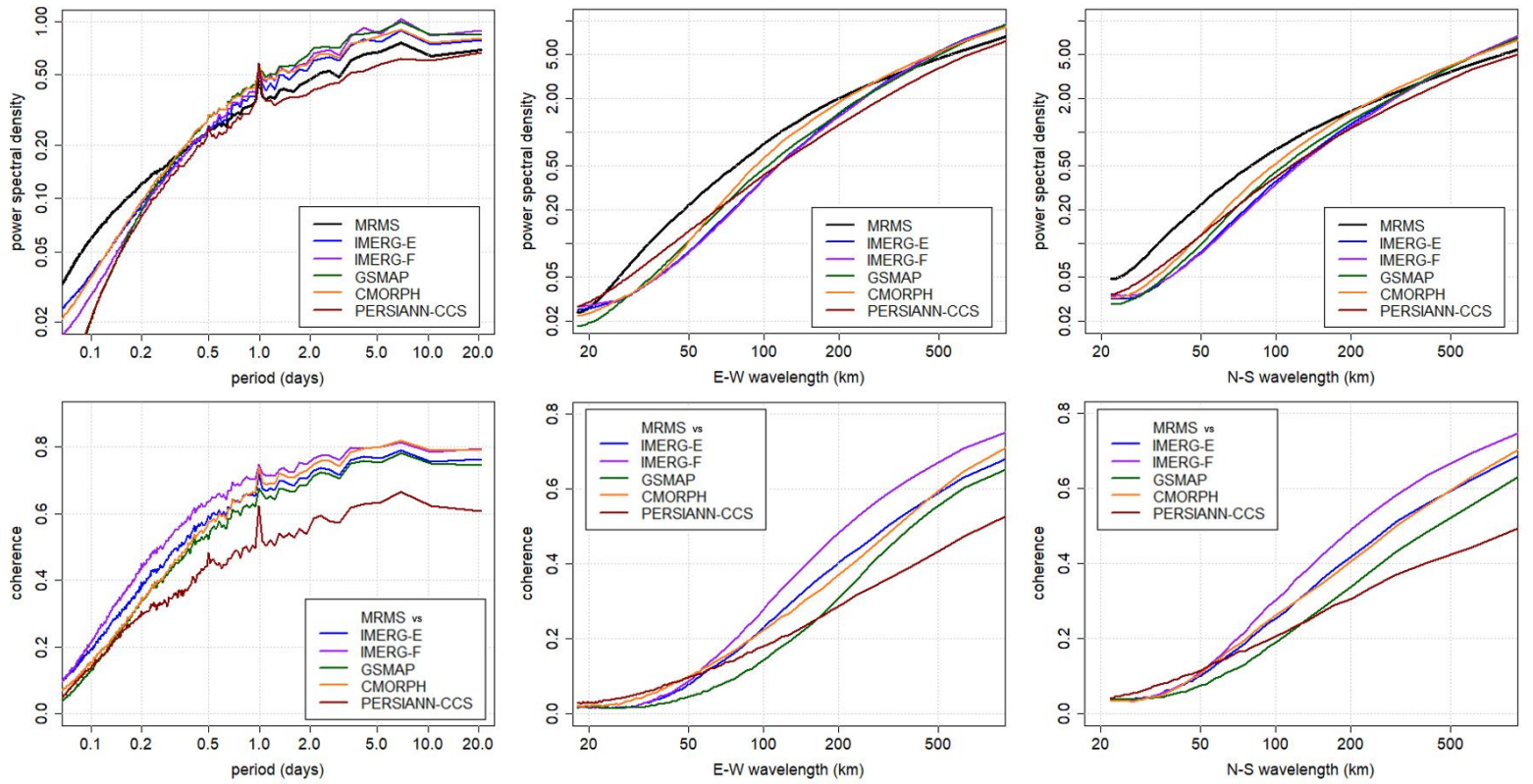
983 of the strongest gradients. In the right panels, most of the spectral power is associated with negative  
984 wavelengths (eastward propagation); the spectral power is concentrated along the lines  
985 corresponding to 40 km/h to 90 km/h velocity. In all panels, smoothed isocontours are added at  
986  $10^0$ ,  $10^{-1}$ ,  $10^{-2}$ ,  $10^{-3}$  and  $10^{-4}$  for enhanced visualization.



987

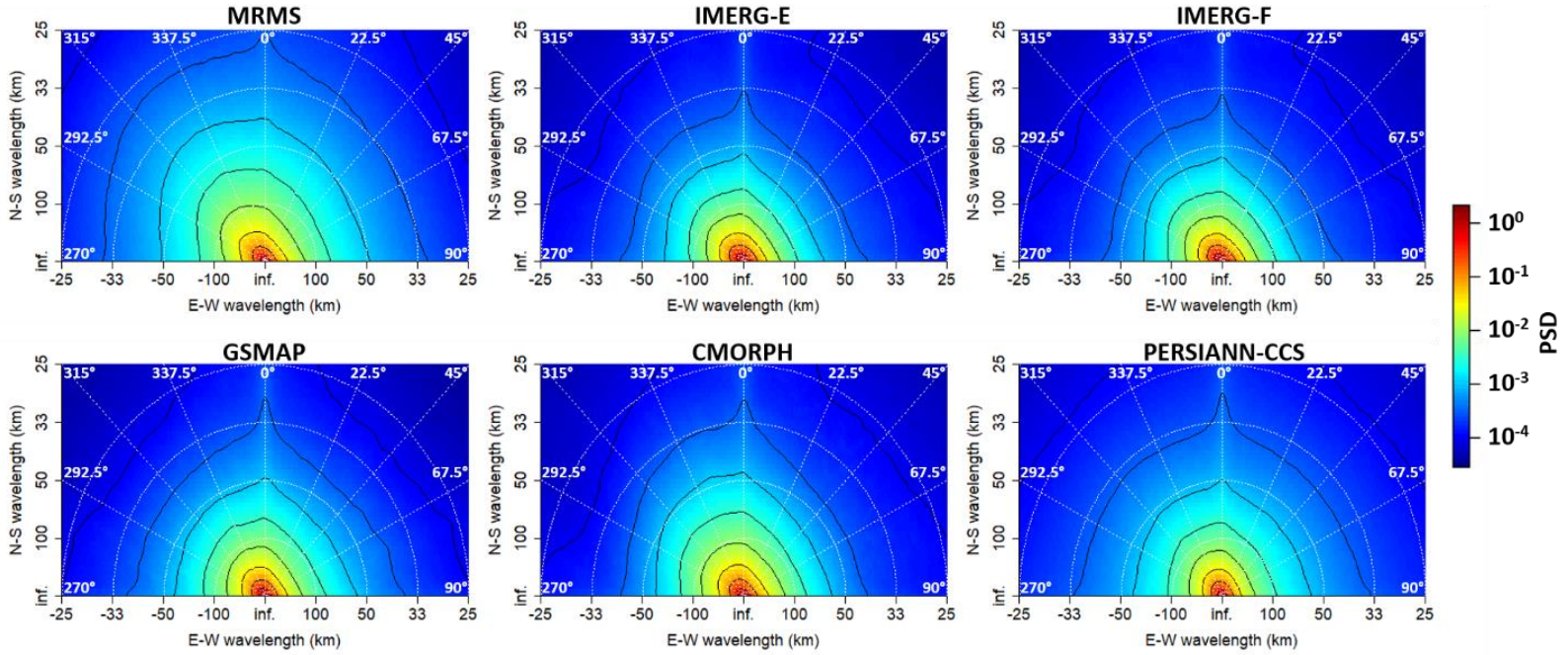
988 **Figure 4: Consistency between GV-MRMS and the satellite products in terms of timing and**  
 989 **location of the precipitation features as functions of spatial wavelengths and temporal period**  
 990 **revealed by the spectral coherence for the storm system in Figure 2. Spectral coherence**  
 991 **(modulus) between GV-MRMS and IMERG and between GV-MRMS and PERSIANN-CCS**  
 992 **computed over the southeastern US from 1900 UTC 2 May 2018 to 0800 UTC 4 May 2018, as a**  
 993 **function of E-W and N-S spatial wavelengths (left), and as a function of the E-W spatial**  
 994 **wavelength and of the temporal period (right). IMERG-F accurately captures the gradients in the**  
 995 **directions between 290° and 320° down to the 50 km wavelength and the features propagating**  
 996 **with a velocity around 60 km/h down to the 2 h time period. PERSIANN-CCS only accurately**

- 997 captures the spatial dynamics down to the 100 km wavelength and down to the 4 h time period. In
- 998 all panels, smoothed isocontours are added at 0.1, 0.2, ..., and 0.9 for enhanced visualization.



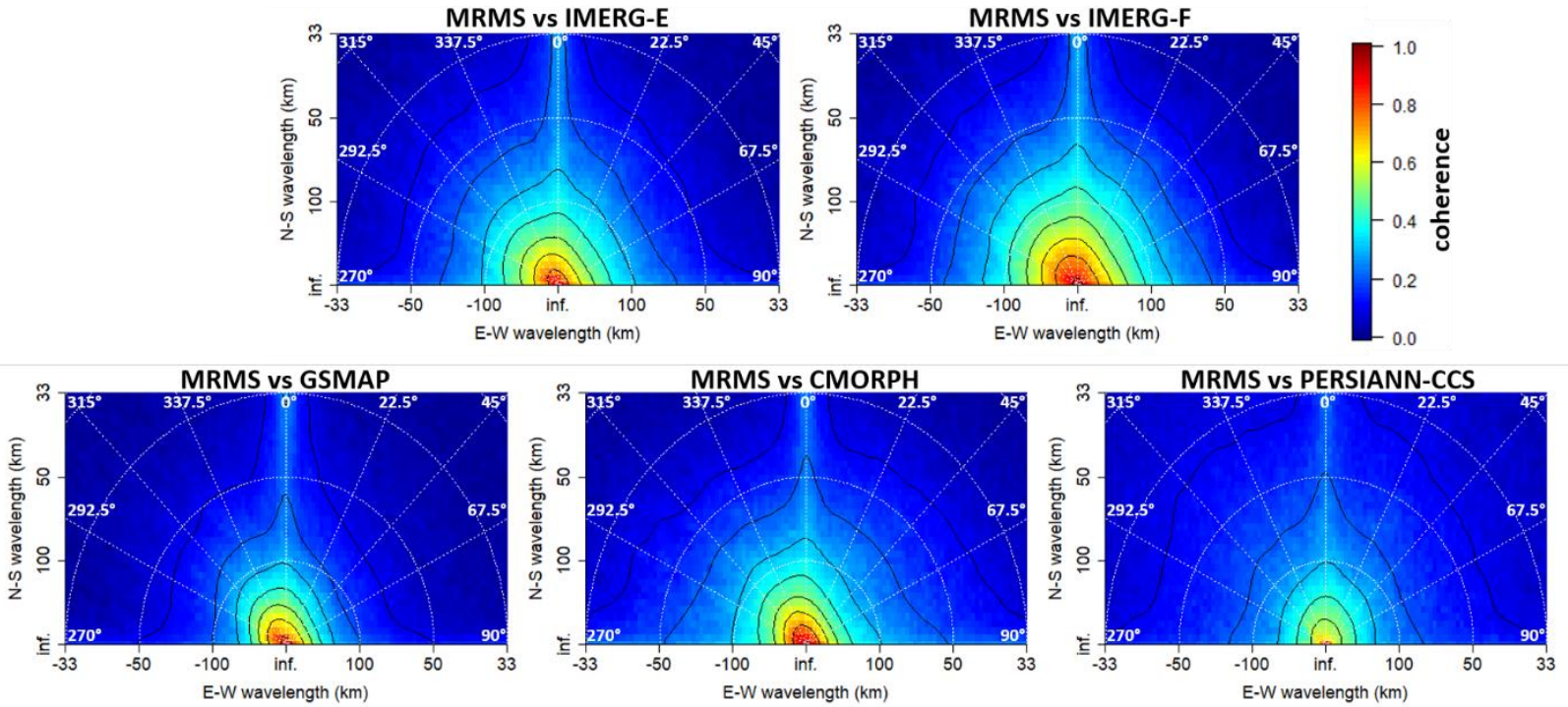
999

1000 **Figure 5: Temporal and spatial dynamics of precipitation over the southeastern US as**  
 1001 **revealed by the marginal PSDs and consistency of the satellite products with GV-MRMS as**  
 1002 **revealed by the spectral coherence.** (top) Marginal temporal (left) and spatial longitudinal and  
 1003 latitudinal (center and right) PSDs of GV-MRMS and satellite precipitation fields from 2018 to  
 1004 2020. (bottom) Spectral coherence (modulus) between the GV-MRMS and satellite precipitation  
 1005 fields as functions of temporal period (left) and spatial wavelengths (center and right). The PSD  
 1006 increasing with longer periods/wavelengths indicates spatially and temporally correlated features  
 1007 with correlation decreasing with time delay and distance. In the left panels, the peak at the 1-day  
 1008 period corresponds to the diurnal cycle. IMERG-F show the highest temporal coherence at all  
 1009 frequencies and highest spatial coherence at wavelengths greater than 70 km.



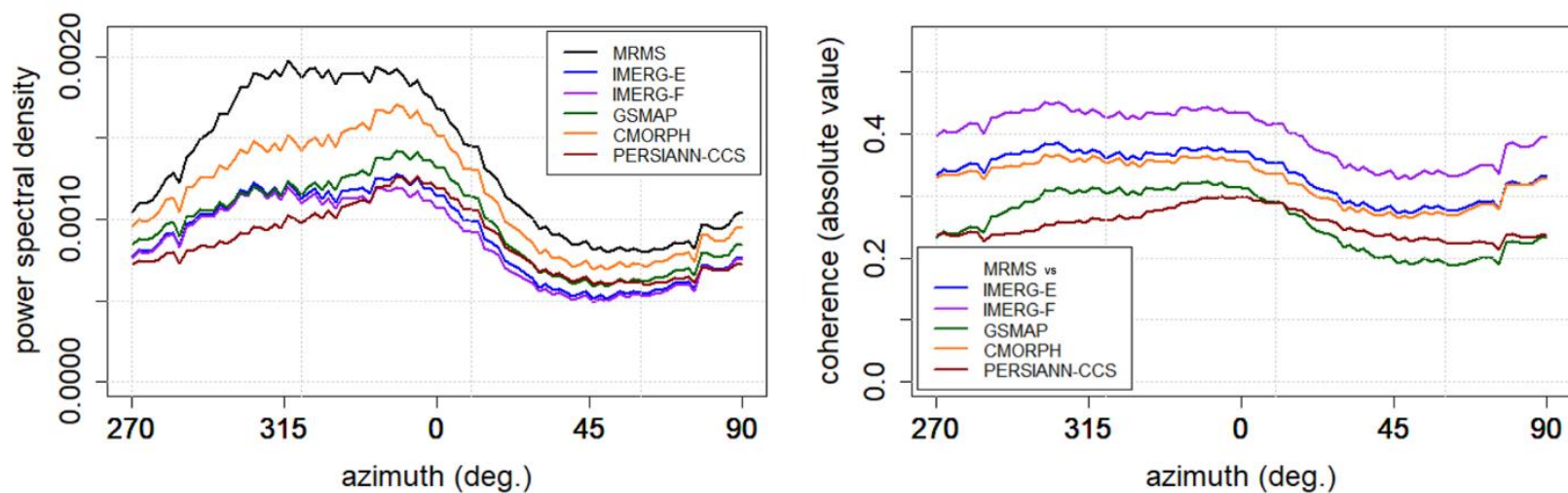
1010

1011 **Figure 6: Average morphology and orientation of precipitation systems over the**  
 1012 **southeastern US as revealed by the 2D spatial PSD.** Joint spatial PSDs of the GV-MRMS and  
 1013 satellite precipitation fields in the N-S and E-W directions. Higher spectral power is found around  
 1014 the 320° direction (approximately NW), which is the direction of the strongest precipitation  
 1015 gradients. In all panels, smoothed isocontours are added at  $10^0$ ,  $10^{-1}$ ,  $10^{-2}$ ,  $10^{-3}$  and  $10^{-4}$  for  
 1016 enhanced visualization.



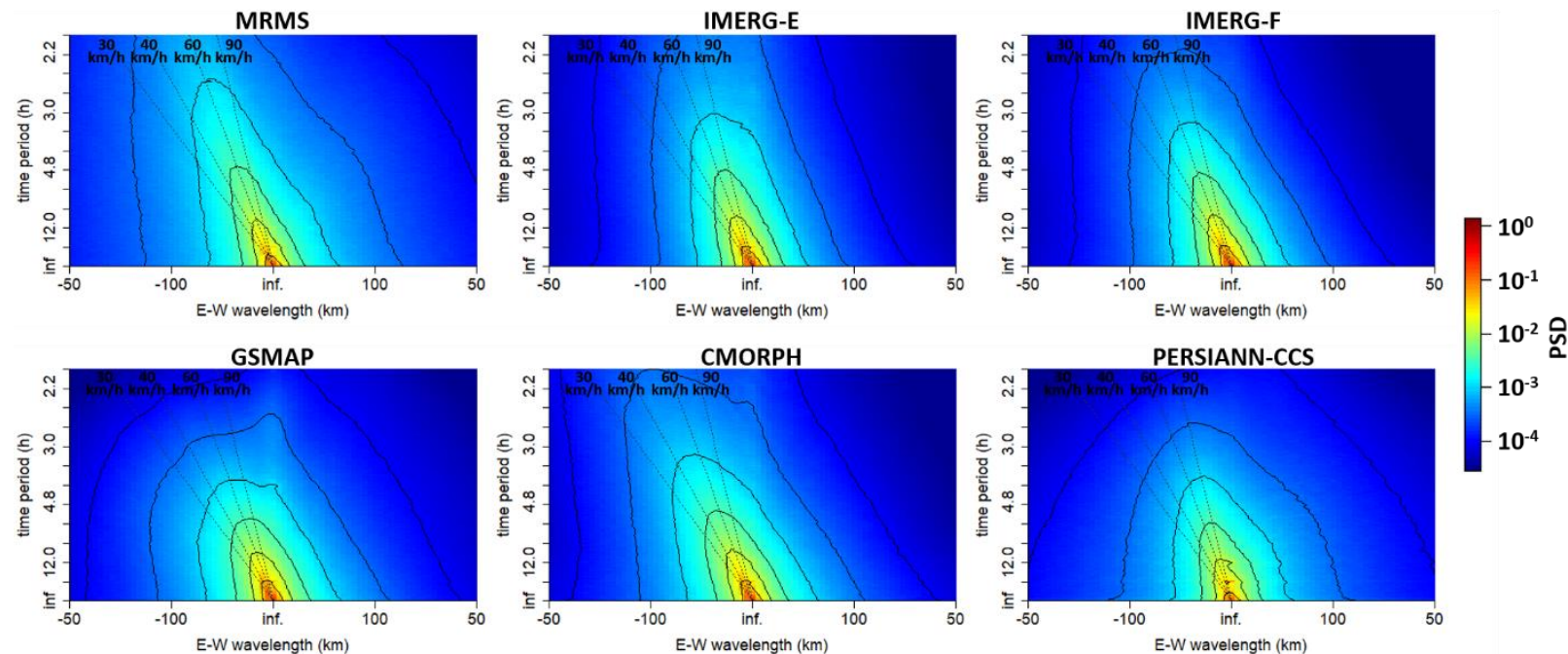
1017

1018 **Figure 7: Ability of the five satellite products to capture the location of precipitation features**  
 1019 **as functions of wavelength and azimuthal direction revealed by the spectral coherence with**  
 1020 **GV-MRMS over the southeastern US.** Spectral coherence (modulus) between the GV-MRMS  
 1021 and satellite precipitation fields as a function of the spatial wavenumbers in the E-W and N-S  
 1022 direction. The direction of the strongest gradients (NW) is also the direction of the highest  
 1023 coherence for all products but PERSIANN-CCS. In all panels, smoothed isocontours are added at  
 1024 0.1, 0.2, ..., and 0.9 for enhanced visualization.



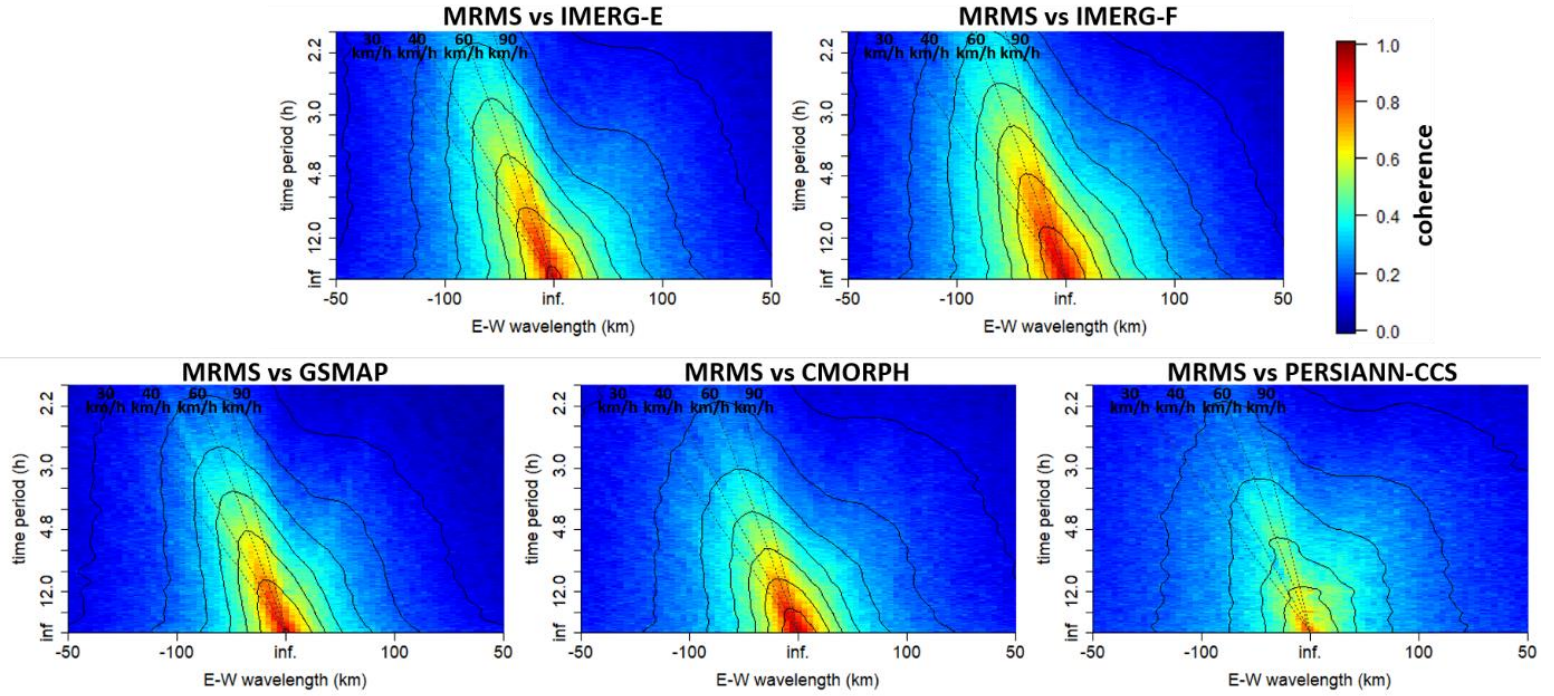
1025

1026 **Figure 8: Spatial variability of precipitation and consistency with GV-MRMS as a function**  
 1027 **of the azimuthal direction for the five satellite products.** (left) PSDs of GV-MRMS and satellite  
 1028 precipitation fields averaged between wavelengths 20 and 300 km as a function of the azimuthal  
 1029 direction. (right) Spectral coherence (modulus) between the GV-MRMS and satellite precipitation  
 1030 fields integrated between wavelengths 20 and 300 km as a function of the azimuthal direction.



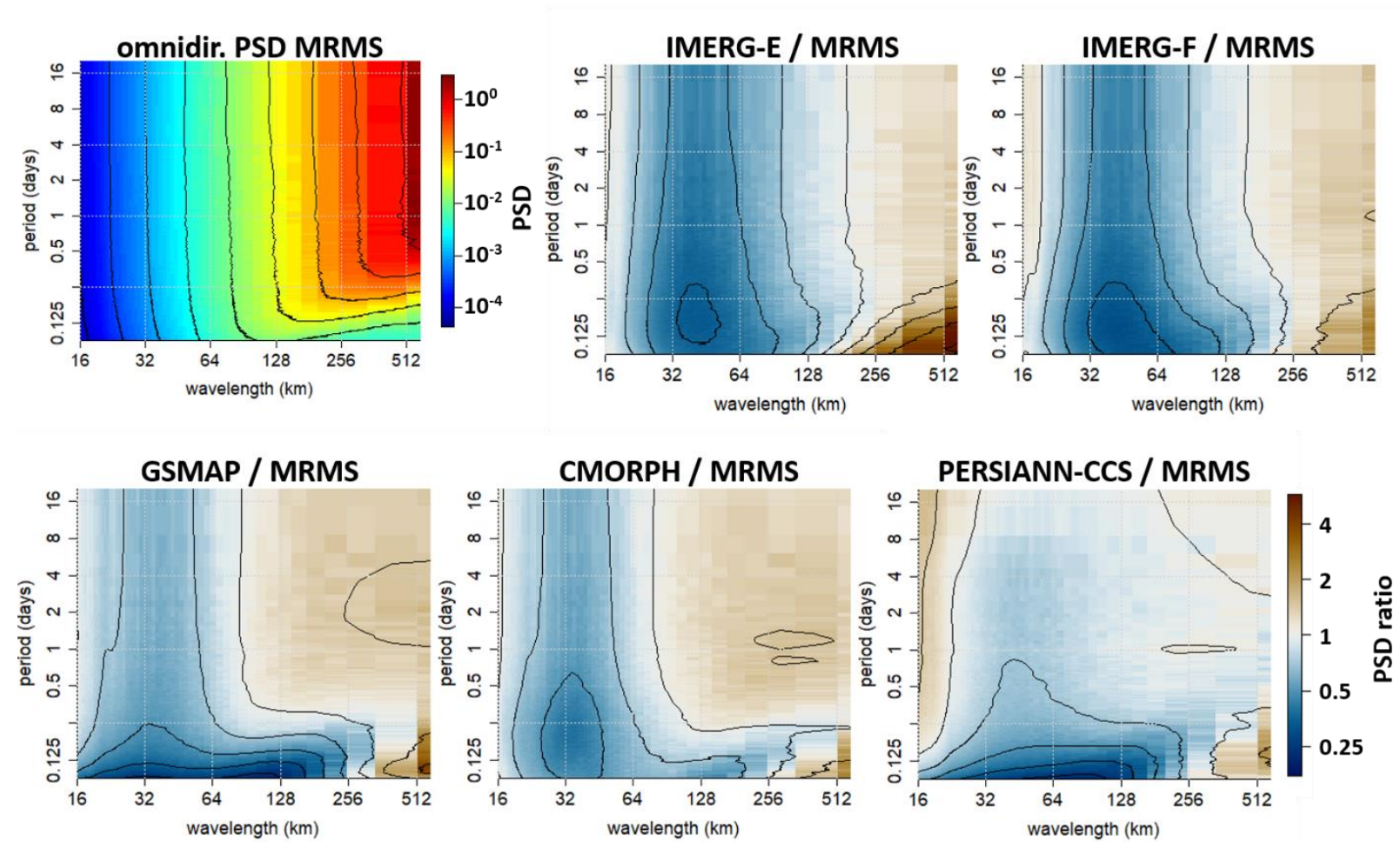
1031

1032 **Figure 9: Dynamics and longitudinal propagation of precipitation over the southeastern US**  
 1033 **as revealed by the E-W space-time PSD.** Joint spatio-temporal PSDs of the GV-MRMS and  
 1034 satellite precipitation fields in the E-W direction. Negative wavelengths correspond to eastward-  
 1035 propagating features and positive wavelengths to westward-propagating features. Most of the  
 1036 spectral power is associated with negative wavelengths (eastward propagation). The dotted lines  
 1037 correspond to non-dispersive eastward propagation with velocity of 30 km/h, 40 km/h, 60 km/h  
 1038 and 90 km/h, from left to right, respectively. In all panels, smoothed isocontours are added at  $10^0$ ,  
 1039  $10^{-1}$ ,  $10^{-2}$ ,  $10^{-3}$  and  $10^{-4}$  for enhanced visualization.



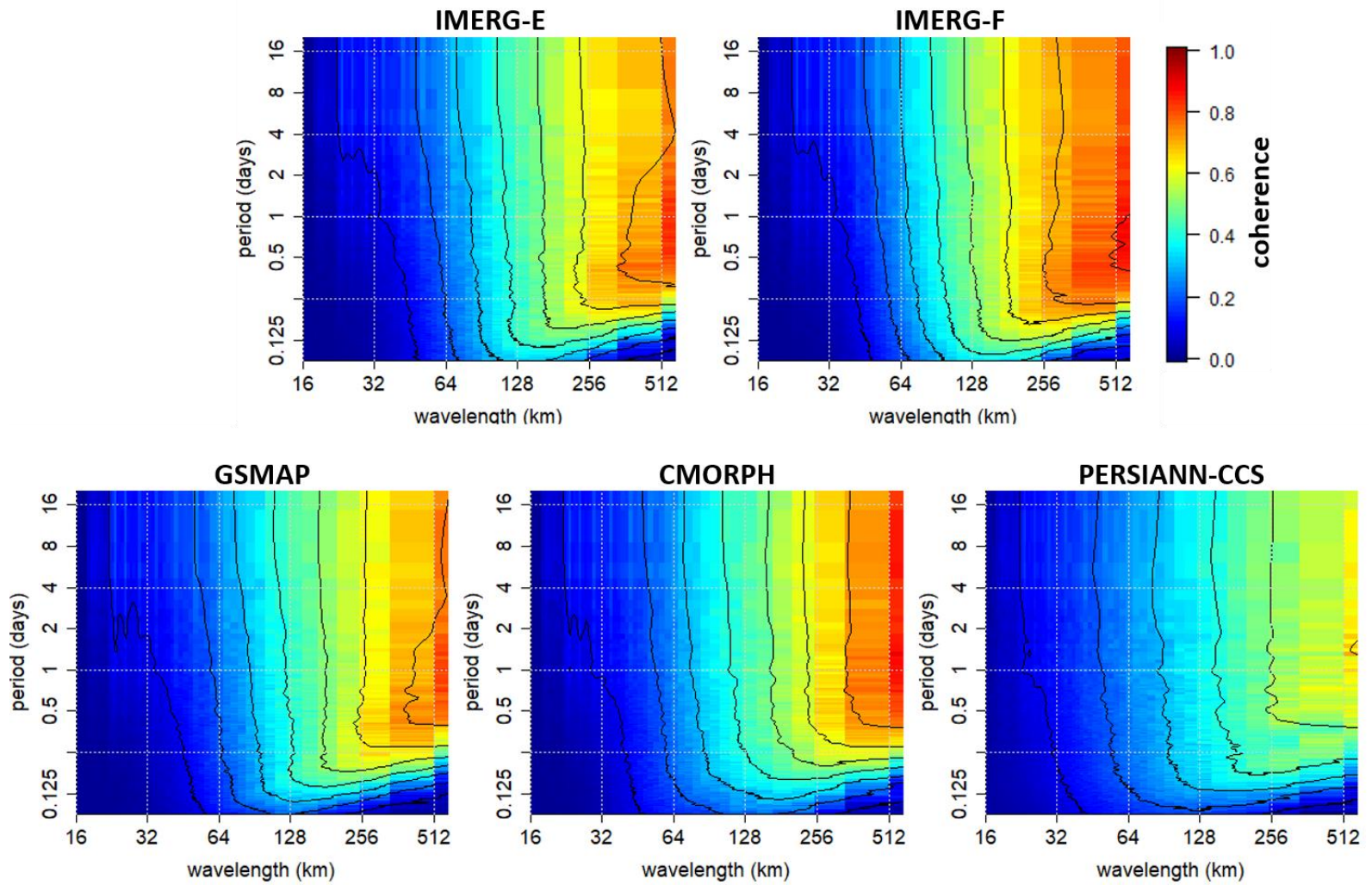
1040

1041 **Figure 10: Ability of the five satellite products to capture location and timing of longitudinal**  
 1042 **propagative precipitation features revealed by the spectral coherence with GV-MRMS over**  
 1043 **the southeastern US.** Spectral coherence (modulus) between the GV-MRMS and satellite  
 1044 precipitation fields as a function of the spatial wavenumber in the E-W direction and of the  
 1045 temporal frequency. The highest coherence corresponds to the dominant eastward propagating  
 1046 features. The dotted lines correspond to non-dispersive eastward propagation with velocity of 30  
 1047 km/h, 40 km/h, 60 km/h and 90 km/h, from left to right, respectively. In all panels, smoothed  
 1048 isocontours are added at 0.1, 0.2, ..., and 0.9 for enhanced visualization.



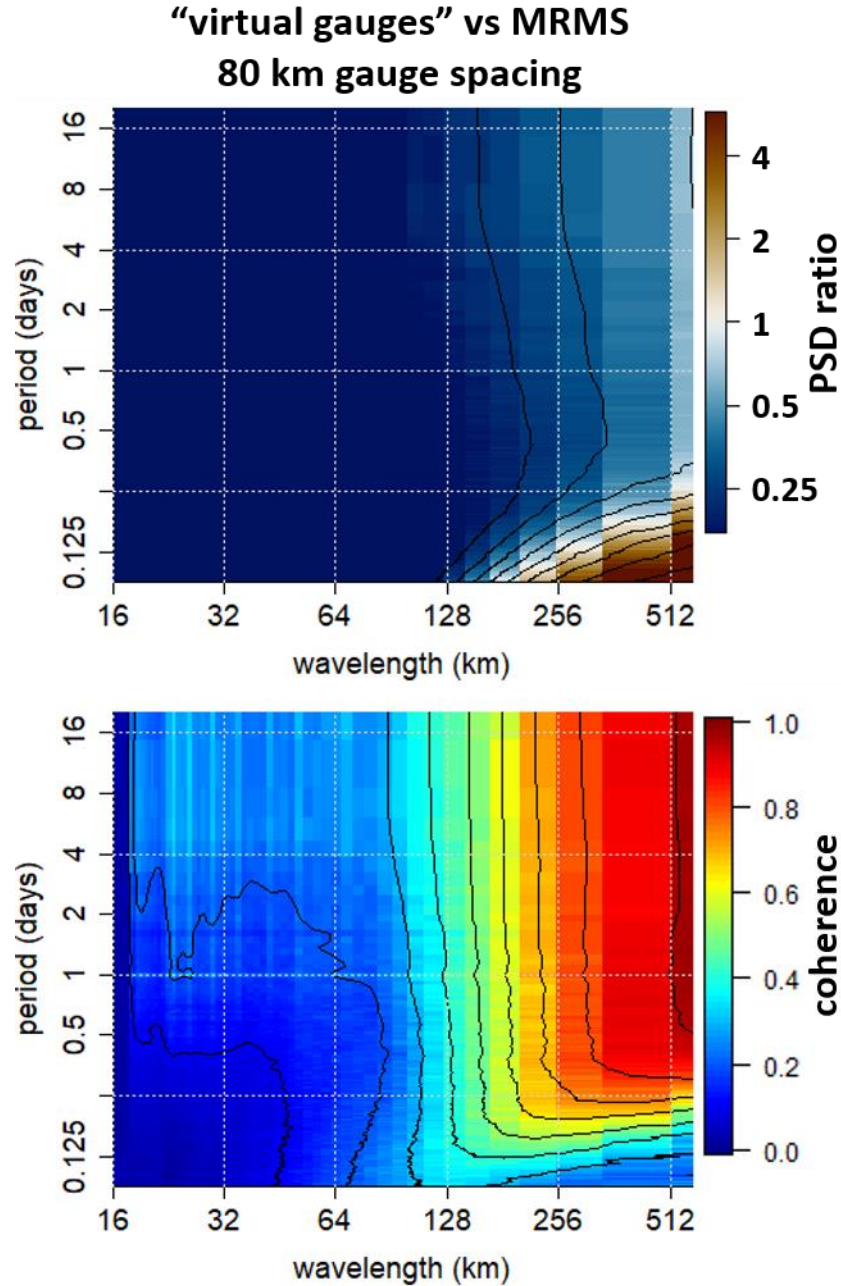
1049

1050 **Figure 11: Comparison of satellite products to GV-MRMS in terms of the distribution of**  
 1051 **spectral power across space-time scales.** (top left) Omnidirectional joint space-time PSD of GV-  
 1052 MRMS precipitation fields. (others) Ratio of the PSD of the satellite products over the PSD of  
 1053 GV-MRMS. Deficit of spectral power in satellite products at short wavelengths (shorter than 100  
 1054 or 200 km) indicates spatially smooth retrieved precipitation fields, i.e. with high spatial  
 1055 correlation at short distances.



1056

1057 **Figure 12: Consistency between GV-MRMS and the satellite products in terms of the timing**  
 1058 **and location of the precipitation features as a function of the spatial wavelength and**  
 1059 **temporal period revealed by the omnidirectional spectral coherence.** Spectral coherence  
 1060 (modulus) between the GV-MRMS and satellite precipitation fields as a function of the  
 1061 omnidirectional spatial wavelength and of the temporal period. For all products, the coherence is  
 1062 below 0.7 at wavelengths shorter than 250 km and periods shorter than 4 h. We consider these fine  
 1063 scales to be unresolved.



1064

1065 **Figure 13: Spectral performance of an idealized gauge network for comparison with the**  
 1066 **satellite products.** (Top) Ratio of the PSD of the interpolated “virtual rain gauges” network with  
 1067 80 km gauge spacing over the PSD of GV-MRMS. (Bottom) Spectral coherence (modulus)  
 1068 between the GV-MRMS and the interpolated “virtual rain gauges” as a function of the  
 1069 omnidirectional spatial wavelength and of the temporal period. By comparison with Figure 12, it

1070 appears that IMERG-F shows spectral performance similar to this theoretical gauge network with  
1071 80 km gauge spacing.